Influence of effective polarization on ion and water interactions within a biomimetic nanopore

Linda X. Phan[1,2], Charlotte I. Lynch[2], Jason Crain[2,3], Mark S.P. Sansom[2], Stephen J. Tucker[1,4*]*

[1] Clarendon Laboratory, Department of Physics, University of Oxford, Oxford, OX1 3PU, UK
[2] Department of Biochemistry, University of Oxford, Oxford, OX1 3QU, UK
[3] IBM Research Europe, Hartree Centre, Daresbury, WA4 4AD, UK
[4] Kavli Institute for Nanoscience Discovery, University of Oxford, OX1 3QU, UK

* To who correspondence should be addressed:

mark.sansom@bioch.ox.ac.uk or *stephen.tucker@physics.ox.ac.uk*

Abstract

Interactions between ions and water at hydrophobic interfaces within ion channels and nanopores are suggested to play a key role in the movement of ions across biological membranes. Previous molecular dynamics (MD) simulations have shown that anion affinity for aqueous/hydrophobic interfaces can be markedly influenced by including polarization effects through an electronic continuum correction (ECC). Here, we designed a model biomimetic nanopore to imitate the polar pore openings and hydrophobic gating regions found in pentameric ligand-gated ion channels. MD simulations were then performed using both a non-polarizable force field and the ECC method to investigate the behavior of water, Na^+ and Cl^- ions confined within the hydrophobic region of the nanopore. Number density distributions revealed preferential Cl^- adsorption to the hydrophobic pore walls, with this interfacial layer largely devoid of Na^+. Free energy profiles for Na^+ and Cl^- permeating the pore also display an energy barrier reduction associated with the localization of Cl^- to this hydrophobic interface, and the hydration number profiles reflect a corresponding reduction in the first hydration shell of Cl^-. Crucially, these ion effects were only observed through inclusion of effective polarization which therefore suggests that polarizability may be essential for an accurate description for the behavior of ions and water within hydrophobic nanoscale pores, especially those that conduct Cl^-.

Statement of Significance

We cannot directly visualize the behavior of water and ions inside channels. However, we can simulate it by using the laws of physics. Current methods are predominantly based on classical (Newtonian) mechanics, but more advanced methods are required if we are to accurately tease apart these complex and dynamic interactions. In this study we show that including the polarization of atoms within our simulations profoundly influences the behavior of anions within a model nanopore. This has implications for our understanding of permeation in Cl- selective ion channels.

Introduction

The interactions of ions and water with membrane-embedded nanopores is of significant biological and technological importance. Nanopores in technology span a wide range of applications including water desalination, DNA sequencing and biosensing, all of which exploit their ability to conduct and often differentiate between charged ions (1, 2). In biology, ion channel pores typically have an internal radius of ~ 0.5 nm and a length of ~ 3 nm. They are responsible for enabling and regulating the movement of ions across lipid bilayers and so can be considered as nanoscale devices (3). Physiological processes rely on their correct functioning, and many diseases (channelopathies) result from their malfunction (4). The importance of understanding both biological ion channel and synthetic nanopore function has therefore led to a sustained interest in the molecular behaviour of ions and water in such nanoconfined environments (5). Yet despite many previous studies, contradictory trends in the many energetic contributions to anionic and water interactions with hydrophobic interfaces (6, 7) has prevented a universal consensus on these influences from being reached.

Ion and water permeation through subnanometer pores is not only influenced by pore radius, but also by the local hydrophobicity of the pore lining. Permeation may readily occur through polar regions with dimensions just larger than the radius of the permeating species (8). However, for hydrophobic regions of comparable dimensions, nanopores may spontaneously dewet, leading to an associated energetic barrier to permeation without steric occlusion (8, 9). This concept is referred to as hydrophobic gating (8, 10, 11) and has been demonstrated in both biological (10, 12–15) and synthetic nanopores (16, 17). A number of recent structural studies have also indicated that hydrophobic surfaces within channels and nanopores may provide favorable interaction sites for anions such as Cl^- that can influence the functional properties of these pores (18, 19). Therefore, an accurate description of the interactions of ions and water with hydrophobic interfaces is essential for the understanding of ion permeation in the confined environments found in such pores.

Extensive studies have been carried out on electrolyte solutions at hydrophobic interfaces such as the aqueous/air interface (6) where molecular dynamics (MD) simulations employing explicitly polarizable force fields have revealed a propensity for halide ions to associate at the interface following the Hofmeister series, i.e. $F^{-} < Cl^{-} < Br^{-} < I^{-}$. This order is directly correlated to the polarizability of the anion so that smaller 'hard' F^{-} ions are excluded from the aqueous/air interface, whereas the larger polarizable halides demonstrate an increasing affinity towards the interface (6, 20–22). Notably, the anion of most biological significance, Cl^{-} , falls in the middle of this series and so its behavior in simulations is likely to be sensitive to the treatment of such interfacial interactions.

Direct experimental observations of ion behavior in interfacial regions remains a challenge. However, interfacial ion properties can be inferred from spectroscopic techniques able to sample surface regions of electrolyte solutions, which can elucidate the hydrogen bonding environment and probe surface ion concentrations (6, 28, 29). These experimental results are largely in agreement with simulation, but nevertheless the quantitative extent of anion adsorption to the aqueous/air interface continues to be a matter of discussion (30).

MD simulations are therefore a useful tool to provide a molecular interpretation that complements such experimental measurements. Many MD studies of nanopores and interfaces employ classical, non-polarizable (NP) force fields which do not fully capture the electronic response to the local environment (31). Neglecting polarizability has consequences for accurately modelling the properties of polarizable anions where many key effects of these ions arise from their electronic responses. For example, the use of NP force fields can lead to inaccuracies in describing short-range ion-water and ion-ion interactions as well as overestimating ion clustering (32, 33).

It has been suggested by Leontyev & Struchebrukhov (34), and expanded upon by Jungwirth *et al.* (26, 35–37), that the lack of polarization and insufficient screening in NP force fields can be compensated for by implicitly accounting for electronic polarization effects through an electronic continuum correction (ECC). The electrostatics of the system may be treated in this way because the linear approximation to polarization may be partitioned into two components: the electronic and orientational polarizations (34, 39). The orientational polarizations are already incorporated into the parameterizations of NP force fields however the electronic polarization is neglected. This becomes a problem for systems involving highly polar media such as water. In practice, the ECC method attempts to reintroduce electronic polarization and charge screening effects in a mean-field approach by rescaling integer charges on monatomic ions in aqueous electrolytes by a factor of $1/\varepsilon_{el}{}^{1/2}$ (26, 34, 38). Here, ε_{el} represents the electronic component of the dielectric constant which can be estimated as the high-frequency dielectric constant of the medium (ε_{el} = 1.78 for water and $\varepsilon_{el} \sim 2$ for proteins). This mean-field approach is physically well-justified and applicable for systems with media of roughly homogenous electronic response i.e., the values of ε_{el} for each media in a system are comparable (37).

The ECC method maintains the computational efficiency of NP force fields whilst able to effectively capture a more physically accurate molecular description without requiring higher level chemical accuracy and the computational costs associated with that. The approach has been widely applied to a range of systems. For example, aqueous/hydrophobic interfaces are especially suited to the use of ECC as the ε_{el} is considered approximately uniform across the system (26, 37). Vazdar *et al.* demonstrated that when ECC is applied to an aqueous/oil interface, there is significant improvement in bulk aqueous salt solution properties relative to NP force field simulations, yielding simulation results in agreement with experimental findings and also comparable to explicitly polarizable force fields (26). These improvements to the ion force field are critical for studies concerning the dynamics of weakly polarizable anions, especially Cl^- . Furthermore, the ECC method has shown promising results when extended to biomolecules (e.g. proteins, lipids, etc.) (37, 40) and even demonstrated equivalent ion occupancy in a potassium channel as an explicitly polarizable force field (41). A common alternative approach to mimic polarizability effects in NP force fields are NBFIX corrections which are applied to CHARMM force fields. These involve ad hoc readjustments to pair-specific LJ parameters to override Lorentz−Berthelot combination rules which aim to reproduce experimentally determined osmotic pressures (42).

The precise mechanism that underlies Cl^- selectivity in nanopores and channels is also poorly understood, and Cl^- channels are often less intensively studied than their cation conductive counterparts. Nonetheless, progress has been made with regard to studying anion channels (19, 43, 44). Unlike cation channels that often have high affinity and selectivity, Cl^- channels are often permeable to other anions (45). Furthermore, it is often unclear how interactions between Cl^- and hydrophobic contacts can influence Cl^- selectivity and consequently determine their functional properties.

With the emergence of many new structures for anion selective channels (46–49), our understanding of the aspects influencing Cl^- selectivity mechanisms will unfold and thus provide insight on the possible side effects associated with simulation models and forcefields on molecular interactions. It is therefore of particular importance to investigate the relationship between hydrophobic contacts and the dynamic behavior of ions and water within their pores. An improved understanding of such interactions will also facilitate design of biomimetic nanopores (50). Certain aspects of such pores can be effectively mimicked by simple non-biological structures, for example graphene nanopores and metal-organic structures (2). Carbon nanotubes (CNTs) are also particularly attractive as structural templates because they can imitate many fundamental aspects of such pores including high transport efficiency, tunable pore diameters, functionalization, and well-defined hydrophobic interiors (51–55). The relevant properties of CNT nanopores have been extensively studied, both experimentally and with simulations (54, 56–58).

Here, we designed a simple biomimetic nanopore to explore the dynamics of ion and water interactions under hydrophobic confinement. We then performed MD simulations of the model nanopore with a NP force field and a NP force field with ECC-rescaled ionic charges to investigate the localization of ions and water relative to the internal hydrophobic nanopore interface. Potential of mean force (PMF) calculations also allowed us to examine the free energy landscapes of ions along the long axis of the pore. Finally, we have explored the hydration structure around these ions at various locations within the central hydrophobic section of the pore. We are thus able to compare the behavior of ions and water inside the pore when modelled by a classical NP force field and for ECC-rescaled ionic charges. Our results demonstrate that modelling polarizability quantitatively alters our model of nanopore/ion interactions and will be important for our understanding of ion permeation in general, especially in Cl^- channels.

Methods

Nanopore Models

Pristine armchair (14,14) CNTs were generated and capped with hydrogen atoms to form the hydrophobic pore using the molecular builder, Avogadro (59), and VMD (60). The length of the CNT was ~ 4.7 nm (and therefore capable of spanning the thickness of the membrane) and the internal diameter was ~ 1.4 nm. A smaller armchair (10,10) CNT was built as a template for insertion and restraining of water molecules in selected positions to create the polar regions of the pore. A harmonic restraining potential was applied between the oxygen of the water molecules and the carbon atoms of the CNT pore wall interiors with a force constant of 1200 kJ mol^{-1} nm^{-2} and a maximum distance of 0.143 nm. For simulations investigating the effects of pore radius, (14,14), (16,16) and (18,18) armchair CNTs were used with internal radii of 0.70 nm, 0.83 nm and 0.95 nm respectively. (10,10), (12, 12) and (14,14) armchair CNTs were used as templates for water molecule insertion to create polar regions for the (14,14), (16,16) and (18,18) CNTs respectively. Pore radius profiles of the resultant model nanopores were calculated using the Channel Annotation Package (CHAP) (61).

Molecular Dynamics Simulations

We performed 50 ns atomistic MD simulations of the model nanopore embedded in a POPC (1-palmitoyl-2-oleoyl-*sn*-glycero-3-phosphocholine) bilayer. The nanopore was inserted into the POPC bilayer by the InflateGRO method whereby the nanopore was placed in the membrane and equilibrated (62). The system was then solvated with a 0.50 M NaCl solution. All systems were first equilibrated for 10 ns and this period was not included in analysis. The simulations were carried out using GROMACS 2020 (www.gromacs.org) (63) with the OPLS all-atom force field with united-atom lipids (64) and the SPC/E water model (65). The integration timestep was 2 fs. All bonds were constrained using the LINCS algorithm (66). A Verlet cutoff scheme was applied and long-range electrostatics were treated by the particle mesh Ewald (PME) method (67) with a short-range cutoff of 1 nm and a Fourier spacing of 0.16 nm. Three-dimensional periodic boundary conditions were applied. Simulations were performed in the isothermal-isobaric ensemble. The temperature was maintained at 300 K with a coupling constant of $\tau_t = 0.5$ ps with a Nose-Hoover thermostat. Pressure was maintained semi-isotropically using the Parrinello-Rahman barostat at 1 bar with a coupling constant of $\tau_t = 2.0$ and compressibility of 4.5×10^{-5} bar^{-1}. For simulations exploring the effects of ion concentration, NaCl concentrations from 0.25 M to 1.0 M were considered in 0.25 M increments. Electronic polarization effects were introduced to the system in a mean-field approach by applying the ECC method (26, 35–37). This was realized by rescaling all ionic charges by $1/\varepsilon_{el}{}^{1/2}$ where ε_{el} = 1.78 is the high frequency dielectric constant for water, thereby equating to a scaling factor of 0.75. We have chosen the ECC method (as opposed to NBFIX) as it has previously been used to study halide ion interactions at aqueous/hydrophobic interfaces (see above) whereas NBFIX may require further parameterization. In all simulations, the model nanopore was modelled using an additive force field. Three independent repeats were carried out for each individual parameter combination. Data was analyzed using GROMACS and locally written code using MDAnalysis (68–70).

<u>Umbrella Sampling</u>

Umbrella sampling was performed to obtain one-dimensional potential of mean force profiles for Na^+ and Cl^- ions moving through the model nanopore using both the non-polarizable force field and ECC method. Simulation details were similar to those detailed above. However, to prevent the nanopore from tilting in the bilayer, the carbon atoms of the CNT were placed under a harmonic restraint with a force constant of 1000 kJ mol^{-1} nm^{-2}. Equilibration simulations were performed for 15 ns and the starting configurations for the umbrella windows were produced from the final state of these simulations.

The reaction coordinate was defined as the z-axis which corresponds approximately to the pore axis and direction normal to the lipid membrane. A target ion was relocated to subsequent positions along the z-axis followed by 10 steps of energy minimization to remove any steric clashes between the target ion and surrounding water molecules. A harmonic biasing potential was applied to the z-coordinate of the target ion with a force constant of 1000 kJ mol^{-1} nm^{-2}. Umbrella windows covered the entire length of the model nanopore and up to 1 nm outside the pore. This setup corresponds to 69 windows along the z-axis with a distance of 0.1 nm between successive windows. Each umbrella window was simulated for 10 ns. PMF profiles were obtained through unbiasing with the Weighted Histogram Analysis Method (WHAM) using the Grossfield lab implementation in version 2.0.9 (http://membrane.urmc.rochester.edu/wordpress/?page_id=126"). The first 5 ns of each simulation were discarded as equilibration, meaning that the final PMF profile was calculated from the final 5 ns of the simulation time. Each resulting PMF was zeroed with respect to the environment outside the nanopore. Convergence was assessed by comparing the cumulative free energy profiles computed from 1 ns fractions of simulation time (Fig. S8).

Results & Discussion

Designing a biomimetic nanopore

In designing a model nanopore, we sought to explore the interactions of Cl^{-} with hydrophobic interfaces in a simplified system representative of a biological ion channel. Based on concepts from our previous studies of pentameric ligand-gated ion channels (pLGICs) (12, 18), we set out to construct a model nanopore that could mimic the general charge distributions of different regions inside such channel pores. pLGICs are a family of ion channels that mediate fast neurotransmission (71). Within their pores, a highly conserved hydrophobic pore-lining region is associated with channel gating (12). There are also narrow regions near the entrances of the pore formed by polar and charged residues (10, 72). We therefore mimicked these two regions in a model nanopore built from a CNT.

The polar regions at either mouth of the nanopore were constructed by applying a harmonic restraining potential between a set of water molecules and the interior pore walls near the openings. We chose to build polar regions in this way to avoid bias toward any particular chemistry of the CNT which may influence ion selectivity (73) and aimed to minimize the introduction of multiple different molecular species. Meanwhile, the central internal hydrophobic cavity was left exposed to resemble the hydrophobic gating region and is the region of interest. This central cavity was considered representative of a (nearly) pure hydrophobic environment as modelling the CNT with higher order electronic moments was expected to have negligible effects since charge distributions become delocalized in the aromatic ring network (74). The resultant model nanopore has three defined regions of alternating polarity and hydrophobicity along its pore axis (**Fig. 1A,B**). This pore was then embedded into a phospholipid bilayer to span the thickness of the membrane (~ 4.7 nm) and form a stable membrane-embedded nanopore (**Fig 1C,D**).

Influence of effective polarization

We performed two sets of simulations of model nanopores in the presence of NaCl solution: non-polarizable (NP) using the additive OPLS-AA force field (64) and ECC using the same force field with ECC-rescaled ionic charges. In both cases the SPC/E water model was employed (65). We then derived the number density profiles of the ions and water along and radially to the pore axis. The influence of the internal pore radius and NaCl concentration on the ion and water densities inside the hydrophobic central region of the pore was studied by sampling from a 1 nm thick slice along the z-axis i.e. from z = -0.5 to +0.5 nm for the final 10 ns of each 50 ns simulation.

Radial density profiles of ions when employing ECC-rescaled charges exhibited increased propensity Cl^- association with the hydrophobic pore lining, as indicated by a density peak displaced towards the water/CNT interface (**Fig. 2A**). By comparison, the Na^+ ions are largely excluded from the immediate vicinity of this hydrophobic surface and are localized closer to the pore axis where they remain more fully solvated (**Fig. 2B**). Significantly, these ion distributions (which match those seen in simulations of ions in water nanodroplets (22, 75)) were only observed when implicitly including polarization through the ECC method. This is in marked contrast to simulations with the NP force field in which both anions and cations were equidistant from the hydrophobic pore wall, preferring to reside close to the pore axis where they are more fully solvated (**Fig. 2D & 2E**). Our results can be explained by the breaking of solvation shell symmetry. This can be realized when considering polarizable anions near a hydrophobic surface such as graphene. Anions and cations in the interfacial layer experience an asymmetric and unequal water polarization response which is non-reciprocal on exchange of the sign of the ion (76) and has also been seen in studies using the Drude polarizable force field (30). Furthermore, our results reveal similar surface effects to those observed at the aqueous/decane interfacial system (**Fig. S1** in the Supporting Material) and are in good agreement with earlier studies of aqueous/air interfaces (21, 26, 35) as well as first principles MD and polarizable simulations of NaCl inside CNTs (77–80).

There is some degree of structuring of the ions and water inside these pores. Notably, the water density distributions (**Fig. 2C & 2F**) form a layered structure inside the nanopore with the outmost layer forming an ordered concentric ring and inner layers demonstrating more bulk-like profiles. In simulations with ECC, it is this outermost layer that is shared with Cl^- ions. Comparable structured behavior of water in concentric shells inside pristine CNT porins has previously been reported (16, 81, 82).

Given the pore is open, and ions and water are freely allowed to permeate, the area under the normalized number density curve indicates the total number of particles in the sampling region. At any given salt concentration, there are significantly fewer Na^+ ions present in the hydrophobic core of the nanopore relative to the number of Cl^- (**Fig. 2A,B,D,E**). This observation is more pronounced when applying the NP force field, with virtually no Na^+ present in the hydrophobic core at lower concentrations, suggesting there is competition between Cl^- and Na^+ to occupy regions close to the pore axis where water density is more bulk-like. With the improved electronic description using ECC, an unequal permeability ratio between ions persists, whilst interfacial properties are captured. It is thought that ion pairs of unusually long lifetimes can form within these dimensions (83). In contrast, DFT calculations have suggested two contradictory effects observed in narrow CNTs: interactions with the image charge favors ion insertion, however this also weakens the binding between ions (84). Thus, our understanding of the cotransport of different ion species under nanometer confinement is incomplete.

Cl^- accumulation at the hydrophobic pore wall

We next examined the behavior of ions and water inside model nanopores with different radii using number density calculations to explore the influence of different degrees of confinement (**Fig. 3**). To investigate this, model nanopores with radii (R_{pore}) for the hydrophobic region of approximately 0.70 nm, 0.83 nm and 0.95 nm, were built. These pore dimensions are comparable to the hydrophobic gate of a simplified open-state β-barrel structure (16). All systems were simulated with 0.50 M NaCl solution. Analysis protocols were the same as those detailed for exploring ion and water number density as a function of salt concentration, however these data were now normalized to the surface area of the pore to focus on interfacial effects.

In the ECC simulations, Cl^- clearly accumulates at the hydrophobic nanopore wall and the extent of this phenomenon is approximately consistent across nanopore sizes, indicated by the relative height of the interfacial peaks (**Fig. 3A**). This suggests that in 0.5 M NaCl, the surface propensity of Cl^-

has reached saturation at the interface and any additional ions entering the hydrophobic region contributed to the density of inner, more bulk-like regions. In contrast, no such interfacial ion effects are observed in the NP simulations (**Fig. 3D**). Instead, an increase in pore radius simply yields a gradual increase in Cl^- density, with the interfacial layer still devoid of ions.

Na^+ is excluded from the hydrophobic interface and favors the middle of the pore in all nanopore sizes in both the ECC and NP simulations (**Fig. 3B & 3E**). Given that the smaller Na^+ ions favor being fully solvated, the increase in pore radius, and thus the increase in volume of the bulk-like water regime, enables more Na^+ to retain their hydration shells leading to an increase in number density. These effects are again comparable to those seen at aqueous/air and aqueous/decane interfaces (26, 35).

The water number density profiles remain similar for both NP and ECC simulations. In the smallest nanopore, the water profiles (**Fig. 3C & 3F**) suggest that water is packed more densely towards the axis of the nanopore, whereas in larger nanopores the density of water becomes progressively more bulk-like with the introduction of more annular rings of water as the pore radius increases. Similar water structure and packing inside CNTs has been observed in MD simulations and experimentally using Raman spectroscopy methods (81, 85).

Overall, these results suggest the preferential accumulation of Cl^- ions (alongside exclusion of Na^+ ions) close to the hydrophobic pore walls are effects due to surface electrostatic interactions involving the ion rather than as a consequence of confinement *per se*. The inclusion of polarization effects through ECC appears not only to affect the structure of water and ions inside the nanopore, but also to increase substantially the anion densities near the interfacial layer – an effect that is not observed with NP force fields.

Energetics of ion permeation

The number density profiles indicate that in the central hydrophobic region of the model nanopore, Cl^- interact preferentially with the pore wall. To explore further the influence of these interactions on ion permeation, we estimated free energy profiles along the pore axis for the $R_{pore} = 0.70$ nm nanopore (**Fig. 4**). We examined how the energetics of ion permeation were impacted by the different ion models. To this end umbrella sampling simulations were performed for both the ECC and NP forcefields to obtain symmetrized one-dimensional potentials of mean force (PMF) for both a Na^+ and Cl^- . Convergence analysis indicated the resulting PMF profiles for Cl^- had converged (i.e. taking $\lesssim$1 kJ/mol change between each fraction of time as a sign of convergence) for both ion parameter sets.

For Na^+, both the NP and the ECC simulations yielded PMFs with a broad energetic barrier with a maximum in the center of the nanopore (i.e. at $z = 0$). This barrier height was ~ 6.2 kJ/mol for the NP PMF and was reduced ~ 3-fold relative to this (to ~ 2.0 kJ/mol) for the corresponding ECC PMF. Interestingly, simulations of a PMF for Na^+ along the length of the channel formed by gramicidin A have shown a ~ 3-fold reduction in the central barrier height when comparing CHARMM27 with the AMOEBA polarizable forcefield (86) and a ~ 4-fold reduction comparing CHARMM27 with the CHARMM DRUDE polarizable forcefield (87).

The shape of the Cl^- PMFs is more complex, but overall is preserved between the NP and ECC simulations. In both cases there is an energy barrier of ~8.3 kJ/mol at $z = 2$ nm corresponding to the narrow (radius ~ 0.4 nm; **Fig. 1D**) polar regions at the entrance to the pore. In this region, it is likely that the ions experience steric effects from the restrained water molecules. The energetic penalty in the polar region may additionally be due to the requirement for Cl^- to partially strip its solvation shell, releasing ~ 2 water molecules which are incompletely compensated for by less favorable interactions with the restrained water molecules which form the pore lining in this region (Fig. S2). The height of this barrier is comparable for the NP and ECC PMFs.

For both the NP and ECC Cl^- PMFs there is a broad energetic well centered around z = 0. However, for the NP simulations, this well is ~ +4.6 kJ/mol relative to solution outside the pore, whereas for the ECC simulations the difference (bulk to hydrophobic pore region) is ~ +1 kJ/mol at z = 1 nm rising to +2 kJ/mol in the center. Thus, at z = 1 nm (just inside the hydrophobic central region) Cl^- is stabilized nearly 4-fold in the ECC simulations relative to in the NP simulations. This correlates with previous studies (see discussion above) which have suggested that Cl^- is preferentially stabilized at a water/hydrophobic interface when ECC or a fully polarizable model are employed in simulations. It also agrees with the number density profiles above (**Fig. 2A & 3A**).

Ion hydration within the nanopore

To examine the molecular origin of the differences in energetic profiles in more detail, we considered the changes in ion hydration at different radial locations inside the hydrophobic central region of the nanopore. The hydrophobic region was divided into four sections radially from the axis of the pore up to the pore wall in increments of 0.175 nm (**Fig. 5A**). The following analysis was performed on the final 5 ns of each simulation. For ions present in each region, radial distribution functions (RDFs) were computed between the ion and oxygens in the water molecules, i.e. $g_{ION\text{-}O}(r)$, for both the NP and ECC simulations. Ion-water coordination numbers were obtained by evaluating the cumulative ion-oxygen RDFs up to the first minimum, corresponding to the number of oxygens in the first hydration shell. All RDFs were calculated on systems solvated with 0.50 M NaCl solution and with nanopore radius of 0.70 nm.

The Cl^- -O RDFs display a change in radius of the first hydration shell both between ion models and ion location. For ions outside the pore, the RDFs achieve the positions of first maxima for ECC and NP models at 0.33 nm (**Fig. S4B & S4C**) and 0.32 nm (**Fig. S4B & S4D**) respectively, whilst sharing relatively similar positions for the first minima. Density functional theory calculations report an RDF first peak distance between 0.31 and 0.32 nm which also agrees with experimental data (88, 89). Similar differences have been noted in simulations comparing Cl^- in bulk solution using NP and

Drude polarizable force fields (79). RDFs with the ECC method show a reduction in peak intensity for the first peak which is associated with a difference in coordination number between force fields. Outside the nanopore (i.e. in bulk solution), the coordination number of Cl^{-} is 5.9 for the ECC compared to 7.1 for the NP force field. The ECC value falls within range of values 5.1 – 6.3 predicted by *ab initio* calculations (90–93) and 6.1 reported by first principles MD simulations (78). Earlier neutron scattering data report hydration numbers of 7.0 ± 0.4 (89) whilst other experiments yielded values of 5.5 ± 0.4 (94). Therefore, the coordination numbers for bulk electrolyte predicted in this study from the ECC simulations are consistent with previous theoretical and experimental data. (We note that our normalized RDFs for outside the pore do not reach a value of 1 at large distances. This is due to the simulation box dimensions and the method of calculation which involves water-oxygen atoms from the whole system including near the bilayer-pore complex. Therefore, this is a non-homogeneous system).

The Cl^{-} first hydration number distributions indicated a significant shift towards lower values for ions at the interface of the pore (i.e., within 0.175 nm of the CNT pore wall), attaining an average value of ~ 5 with a significant fraction of ions with hydration numbers of ≤ 4.5 (**Fig. 5B**). In comparison, towards the (radial) center of the nanopore where water density is more bulk-like, the hydration number is on average ~ 6.1. Between the interface and radial center of the pore, the average hydration number ranges within these limits (**Fig. 5B**). The shape of the distributions become progressively broader with increasing distance away from the interface which indicates that the structure of the hydration shell becomes more flexible, approaching more bulk-like water behavior. In comparison, the Cl^{-} hydration shell is less flexible when using the NP force field. This is reflected in the hydration number distributions which remain tighter for NP (**Fig. 5D**) compared to ECC and are centered on an average coordination number of ~ 7.0 in all radial sections inside the nanopore, suggesting the hydration shell remains predominantly intact.

It is interesting also to consider the proportion of time Cl^{-} spends in various regions or, in other words, the percentage occupancy of each radial section (**Fig. 5C**). With ECC, Cl^{-} spends a significantly greater proportion of time in the interfacial layer whereas with the NP force field, Cl^- is more inclined to occupy regions away from the pore wall. These findings align with the number density distributions (**Fig. 2A & 3A**).

In contrast with Cl^- , the RDFs for Na^+ are in good agreement for inside compared to outside (i.e. bulk electrolyte) the pore for the first hydration shell with the ECC force field (**Fig. S3B**), suggesting that Na^+ retains their solvation shell under hydrophobic confinement within these pores. The coordination number of Na^+ at the interface is ~ 4.2, whereas outside the pore (i.e. in the bulk electrolyte) Na^+ has a coordination number of ~ 4.8 when employing ECC (**Fig. S3A**). By contrast, a coordination number of ~ 5.0 is seen for Na^+ regardless of location using the NP force field (**Fig. S3D**). Coordination numbers within the range 4.9–6.1 have previously been predicted for Na^+ in bulk water using *ab initio* methods (90, 95, 96). Older experiments of X-ray and neutron diffraction, and Raman spectroscopy predict coordination numbers between 4–8 for Na^+ in aqueous solution (97). The proportion of frames analyzed with Na^+ present indicated that they were more likely to occupy the space away from the interface (**Fig. S3C & S3F**). These results reinforce the findings from number density calculations.

Overall, using the ECC parameters, Cl^- has a more flexible hydration shell and is more inclined to partially desolvate to favorably interact with the hydrophobic pore wall. Conversely, the Cl^- hydration shell remains predominantly intact using the NP force field and occupies regions away from the interface. Na^+ prefers to remain more solvated by moving through the nanopore closer to the pore axis where the structure of water is more bulk-like relative to the pore wall.

Robustness and sensitivity to the ECC model

There are some variations in the published ECC model (20, 26, 39, 99). Specifically, the more recent ECCR model (99) includes some additional small changes to ionic van der Waals parameters. We therefore compared ion density profiles as a function of radial position for our nanopore models using the ECC model in which only ionic charges have been modified and using the ECCR model in which van der Waals radii were also adjusted. As can be seen from **Fig. S5**, whilst the results show some sensitivity of the details of ion profiles to the model employed, in all cases for three different pore radii, the fundamental basic observation of accumulation of Cl^- ions alongside depletion of Na^+ ions at the hydrophobic wall of the nanopore is observed. Furthermore, in all three pore models, for both the ECC and ECCR treatments, the difference in distribution of ions at the pore wall (calculated as $\Delta r(Cl-Na)$, i.e. the difference in distance from the nanopore wall at which the ionic concentration rises to 50%; see **Fig. S5** for details) is ~ 0.2 nm, i.e. the outermost solvation shell of the nanopore experiences an enhanced local concentration of anions. We are therefore confident that our observations are robust to reasonable variations in the implementation of the ECC model.

To explore this further, we have calculated free energy profiles using the ECCR model following the same simulation protocol as for the ECC and NP PMF calculations. As seen in **Fig. 4** (also see **Fig. S6**) the shape of the Cl^- PMFs are preserved between ECCR, ECC and NP simulations, exhibiting similar notable features corresponding to the polar regions at the pore entrances and a central barrier depletion in the hydrophobic core (z = 0 nm). For Cl^- in the polar regions, the energy barrier for ECCR is ~ 1 kJ/mol less compared to ECC and NP (**Fig. S6A**). This can be attributed to the additional van der Waals radius rescaling applied in ECCR and hence permeating ions likely experience fewer steric clashes. The free energy barrier for Cl^- using the ECCR parameters in the center of the nanopore (z = 0 nm) is ~ 4 kJ/mol which is a little lower than the NP energy at this location. This is perhaps somewhat unexpected given the number density profiles for Cl^- employing ECCR and ECC share similarities associated with the enhanced localization of anions to the hydrophobic pore interface (**Fig. S5**) as discussed previously. For Na^+, an energetic maximum of ~ 3 kJ/mol is reached at z ~ 1 nm (**Fig. S6B**) where the ion begins to move into the hydrophobic core of the nanopore and away from the polar regions. The free energy at z = 0 nm is maintained at ~ 2.5 kJ/mol relative to outside the nanopore. Contrary to the pattern seen with Cl^-, the free energy associated with ECCR for Na^+ is closer to the PMF profile for ECC in the hydrophobic region which corresponds to the comparable number density plots in **Fig. S5**. However, for both ionic species the free energy of ions in the center of the pore follows the order NP > ECCR > ECC. Thus, this additional work highlights the sensitivity of nanoscale effects to ion parameters in MD simulations.

Additional exploration of ECC model sensitivity used an aqueous/decane interface as a simple model slab system (*cf.* (26)). We examined ECC sensitivity in this system to the water model employed, using four widely employed models (SPC/E, TIP3P, TIP4P and TIP4P/2005; see **Fig. S7A**). In all cases, local accumulation of Cl^- and depletion of Na^+ at the hydrophobic interface was seen, but the details of the ion concentration vs. r profiles showed some sensitivity to the water model such that $\Delta r(Cl{-}Na)$ ranged from ~ 0.1 to ~ 0.2 nm. We also made preliminary comparisons with a polarisable model (AMOEBA (102, 103)) which revealed a comparable local accumulation of Cl^- /depletion of Na^+ at the hydrophobic interface with $\Delta r(Cl{-}Na)$ = ~ 0.3 nm (**Fig. S7B**). This is in broad agreement with previous comparisons of ECC with polarisable models (20, 100).

Together these results suggest that our observation of local accumulation of Cl^- at the hydrophobic nanopore wall is robust to variations in the ECC model, and that this model is likely to mimic more computationally demanding polarizable simulations. It is also helpful to consider how well these simulations mimic experimental reality for anions close to a graphene-like hydrophobic surface. A recent study (104) compared anion adsorption to graphene/water interfaces as measured by surface-sensitive spectroscopy with (non-polarizable) MD simulations. This revealed that the experimental free energy of anion adsorption to a water/graphene interface could be reproduced by scaling the anion (iodide) charge by ~ 0.8, as is the case in the ECC model. This in turn suggests that the ECC model is likely to quantitatively reproduce local anion accumulation at the hydrophobic interface of a CNT-derived model nanopore.

Conclusions

In this study, we have designed a model nanopore which mimics aspects of the critical pore region within pLGICs. This allows us to explore the interactions of ions and water in hydrophobically confined environments. Our results underline the importance of including polarization effects to model more accurately the interactions of ions (especially Cl^-) with the hydrophobic surfaces that often line pores of this size. In particular, our findings demonstrate that when using the ECC model, the larger, more polarizable, Cl^- ions preferentially reside in the outermost interfacial layer of the hydrophobic region inside the nanopore, whereas the smaller, ‘hard’ Na^+ ions are repelled from the interface and occupy more bulk-like regions. Using this model, we investigated the effect of NaCl concentration and pore radius on ion localization and report that this trend persists. These observations resemble interfacial effects observed at aqueous/air and aqueous/oil (**Fig. 6B**) interfaces and are not reproduced using the non-polarizable force field (26, 35).

Through analysis of the ion hydration structure inside the hydrophobic core, it has been possible to investigate ion solvation as a function of radial position from the pore axis. A Cl^- in proximity of the hydrophobic pore wall can be seen to partially lose its hydration shell to form favorable interactions with the hydrophobic wall of the pore (**Fig. 6A**). This behavior is not captured without inclusion of polarization effects. Conversely, as Na^+ ions dominantly occupy bulk-like regions, their solvation shell remains largely intact.

Free energy profiles for ions correlate with their number density profiles. The PMF profile for Cl^- with ECC suggests the partial loss of its hydration shell is energetically advantageous whereas the barrier for Na^+ is higher. Therefore, this suggests that the hydrophobic core of the nanopore exhibits a degree of selectivity for Cl^- over Na^+. Comparable Cl^- −hydrophobic interactions have recently been reported in biological Cl^- channels and transport proteins, for example in the NTQ Cl^- -pumping rhodopsin (PDB: 5G28) (105) and in the bestrophin-1 chloride channel (PDB: 4RDQ) (106). Similarly, some synthetic anionphores (biotin[6]uril hexaesters) exploit C—H hydrogen bond donors to selectively transport softer anions over harder, more basic anions (107). Thus, it is important to model accurately the interactions of anions with hydrophobic binding sites in channels, transporters, and synthetic carriers. In this context, it is of interest that Orabi *et al.* (33) have explored the effects modifying ion van der Waals parameters using NBFIX to mimic polarizability effects in simulations of a CLC Cl⁻ transporter. Their results demonstrated that with the standard CHARMM36m force field, Cl⁻ experienced dissociation from the binding site observed in the crystal structure of the protein, whereas the ion remains bound with the NBFIX parameters. Taken together, these studies indicate that further investigation is required into how the inclusion of electronic polarizability in simulations may influence our understanding of anion behavior in both synthetic and biological anion selective structures.

Overall, our analysis of a model biomimetic nanopore reveals contrasting ion behavior that may provide insights into the fundamental principles of anion selectivity and has the potential to influence technological applications. Our findings also suggests that the inclusion of electronic polarizability in ion modelling is key to accurately capturing Cl⁻ behavior. Moreover, this current study contributes to the longstanding debate over force field accuracy and whether more explicit treatment of electrostatics is necessary at the expense of computational efficiency (108, 109). With the evolution of better and more powerful computational resources, more extensive simulations comparing interactions between Cl⁻ and hydrophobic interfaces using explicitly polarizable force fields and even quantum mechanical methods may therefore provide new mechanistic insights into anion permeation and selectivity.

Author Contributions

LX-P and CIL performed research and analyzed data. All authors designed research and wrote the paper. SJT, JC and MSPS obtained funding for the project.

Declaration of Interest

JC is an Employee of IBM Research. All other authors have no interests to declare.

Acknowledgements

This work was supported by grants from the BBSRC and the EPSRC and by an EPSRC iCASE studentship award in collaboration with IBM Research to LXP. It was also supported by the Hartree National Centre for Digital Innovation - a collaboration between the Science and Technologies Facilities Council and IBM.

References

1. Corry, B. 2008. Designing Carbon Nanotube Membranes for Efficient Water Desalination. *J. Phys. Chem. B*. 112:1427–1434.
2. Prasad K, V., S.K. Kannam, R. Hartkamp, and S.P. Sathian. 2018. Water desalination using graphene nanopores: Influence of the water models used in simulations. *Physical Chemistry Chemical Physics*. 20:16005–16011.
3. Hille, B. 2001. Ionic Channels of Excitable Membranes. 3rd ed. Sinauer Associates Inc.
4. Ashcroft, F. 2000. Ion Channels and Disease. San Diego : Academic Press.
5. Lynch, C.I., S. Rao, and M.S.P. Sansom. 2020. Water in Nanopores and Biological Channels: A Molecular Simulation Perspective. *Chemical Reviews*. 120:10298–10335.
6. Tobias, D.J., A.C. Stern, M.D. Baer, Y. Levin, and C.J. Mundy. 2013. Simulation and Theory of Ions at Atmospherically Relevant Aqueous Liquid-Air Interfaces. *Annual Review of Physical Chemistry*. 64:339–359.
7. Levin, Y., and A.P. dos Santos. 2014. Ions at hydrophobic interfaces. *Journal of Physics Condensed Matter*. 26:203101.
8. Rao, S., G. Klesse, P.J. Stansfeld, S.J. Tucker, and M.S.P.P. Sansom. 2019. A heuristic derived from analysis of the ion channel structural proteome permits the rapid identification of hydrophobic gates. *Proceedings of the National Academy of Sciences of the United States of America*. 116:13989–13995.
9. Beckstein, O., and M.S.P. Sansom. 2003. Liquid-vapor oscillations of water in hydrophobic nanopores. *Proceedings of the National Academy of Sciences of the United States of America*. 100:7063–7068.
10. Aryal, P., M.S.P. Sansom, and S.J. Tucker. 2015. Hydrophobic gating in ion channels. *Journal of Molecular Biology*. 427:121–130.
11. Beckstein, O., P.C. Biggin, and M.S.P. Sansom. 2001. A hydrophobic gating mechanism for nanopores. *Journal of Physical Chemistry B*. 105:12902–12905.
12. Rao, S., G. Klesse, C.I. Lynch, S.J. Tucker, and M.S.P. Sansom. 2021. Molecular Simulations of Hydrophobic Gating of Pentameric Ligand Gated Ion Channels: Insights into Water and Ions. *Journal of Physical Chemistry B*. 125:981–994.
13. Rao, S., G. Klesse, P.J. Stansfeld, S.J. Tucker, and M.S.P. Sansom. 2017. A BEST example of channel structure annotation by molecular simulation. *Channels*. 11:347–353.
14. Rao, S., C.I. Lynch, G. Klesse, G.E. Oakley, P.J. Stansfeld, S.J. Tucker, and M.S.P. Sansom. 2018. Water and hydrophobic gates in ion channels and nanopores. *Faraday Discussions*. 209:231–247.
15. Lynch, C.I., G. Klesse, S. Rao, S.J. Tucker, and M.S.P. Sansom. 2021. Water Nanoconfined in a Hydrophobic Pore: Molecular Dynamics Simulations of Transmembrane Protein 175 and the Influence of Water Models. *ACS Nano*.
16. Trick, J.L., E.J. Wallace, H. Bayley, and M.S.P. Sansom. 2014. Designing a hydrophobic barrier within biomimetic nanopores. *ACS Nano*. 8:11268–11279.
17. Powell, M.R., L. Cleary, M. Davenport, K.J. Shea, and Z.S. Siwy. 2011. Electric-field-induced wetting and dewetting in single hydrophobic nanopores. *Nature Nanotechnology*. 6:798–802.
18. Klesse, G., S. Rao, S.J. Tucker, and M.S.P.P. Sansom. 2020. Induced Polarization in Molecular Dynamics Simulations of the 5-HT3 Receptor Channel. *Journal of the American Chemical Society*. 142:9415–9427.
19. Ruan, Z., I.J. Orozco, J. Du, and W. Lü. 2020. Structures of human pannexin 1 reveal ion pathways and mechanism of gating. *Nature*. 584:646–651.
20. Jungwirth, P., and D.J. Tobias. 2001. Molecular structure of salt solutions: A new view of the interface with implications for heterogeneous atmospheric chemistry. *Journal of Physical Chemistry B*. 105:10468–10472.
21. D’Auria, R., and D.J. Tobias. 2009. Relation between surface tension and ion adsorption at the air-water interface: A molecular dynamics simulation study. *Journal of Physical Chemistry A*. 113:7286–7293.
22. Thaunay, F., G. Ohanessian, and C. Clavaguéra. 2017. Dynamics of ions in a water drop using the AMOEBA polarizable force field. *Chemical Physics Letters*. 671:131–137.
23. Levin, Y., A.P. dos Santos, and A. Diehl. 2009. Ions at the air-water interface: An end to a hundred-year-old mystery? *Physical Review Letters*. 103:1–4.
24. Levin, Y. 2009. Polarizable ions at interfaces. *Physical Review Letters*. 102:1–4.
25. Petersen, P.B., and R.J. Saykally. 2006. On the Nature of Ions At the Liquid Water Surface. *Annual Review of Physical Chemistry*. 57:333–364.

26. Vazdar, M., E. Pluhařová, P.E. Mason, R. Vácha, and P. Jungwirth. 2012. Ions at hydrophobic aqueous interfaces: Molecular dynamics with effective polarization. *Journal of Physical Chemistry Letters*. 3:2087–2091.
27. dos Santos, A.P., and Y. Levin. 2012. Ions at the water-oil interface: Interfacial tension of electrolyte solutions. *Langmuir*. 28:1304–1308.
28. Garrett, B.C. 2004. Ions at the Air/Water Interface. *Science*. 303:1146–1147.
29. Piatkowski, L., Z. Zhang, E.H.G. Backus, H.J. Bakker, and M. Bonn. 2014. Extreme surface propensity of halide ions in water. *Nature Communications*. 5:1–7.
30. Son, C.Y., and Z.-G. Wang. 2021. Image-charge effects on ion adsorption near aqueous interfaces. 118:1–8.
31. Benavides, A.L., M.A. Portillo, V.C. Chamorro, J.R. Espinosa, J.L.F. Abascal, and C. Vega. 2017. A potential model for sodium chloride solutions based on the TIP4P/2005 water model. *Journal of Chemical Physics*. 147.
32. Bruce, E.E., and N.F.A. van der Vegt. 2018. Does an electronic continuum correction improve effective short-range ion-ion interactions in aqueous solution? *Journal of Chemical Physics*. 148:1–12.
33. Orabi, E.A., T.N. Öztürk, N. Bernhardt, and J.D. Faraldo-Gómez. 2021. Corrections in the CHARMM36 Parametrization of Chloride Interactions with Proteins, Lipids, and Alkali Cations, and Extension to Other Halide Anions. *Journal of Chemical Theory and Computation*. 17:6240–6261.
34. Leontyev, I. v., and A.A. Stuchebrukhov. 2009. Electronic continuum model for molecular dynamics simulations. *Journal of Chemical Physics*. 130:1–8.
35. Jungwirth, P., and D.J. Tobias. 2006. Specific ion effects at the air/water interface. *Chemical Reviews*. 106:1259–1281.
36. Pluhařová, E., H.E. Fischer, P.E. Mason, and P. Jungwirth. 2014. Hydration of the chloride ion in concentrated aqueous solutions using neutron scattering and molecular dynamics. *Molecular Physics*. 112:1230–1240.
37. Duboue-Dijon, E., M. Javanainen, P. Delcroix, P. Jungwirth, and H. Martinez-Seara. 2020. A practical guide to biologically relevant molecular simulations with charge scaling for electronic polarization. *Journal of chemical physics*. 153:1–15.
38. Leontyev, I., and A. Stuchebrukhov. 2011. Accounting for electronic polarization in non-polarizable force fields. *Physical Chemistry Chemical Physics*. 13:2613–2626.
39. Kirby, B.J., and P. Jungwirth. 2019. Charge Scaling Manifesto: A Way of Reconciling the Inherently Macroscopic and Microscopic Natures of Molecular Simulations. *Journal of Physical Chemistry Letters*. 10:7531–7536.
40. Melcr, J., H. Martinez-Seara, R. Nencini, J. Kolafa, P. Jungwirth, and O.H.S. Ollila. 2018. Accurate Binding of Sodium and Calcium to a POPC Bilayer by Effective Inclusion of Electronic Polarization. *Journal of Physical Chemistry B*. 122:4546–4557.
41. Jing, Z., J.A. Rackers, L.R. Pratt, C. Liu, S.B. Rempe, and P. Ren. 2021. Thermodynamics of ion binding and occupancy in potassium channels. *Chemical Science*.
42. Tolmachev, D.A., O.S. Boyko, N. v. Lukasheva, H. Martinez-Seara, and M. Karttunen. 2020. Overbinding and Qualitative and Quantitative Changes Caused by Simple Na+ and K+ Ions in Polyelectrolyte Simulations: Comparison of Force Fields with and without NBFIX and ECC Corrections. *Journal of Chemical Theory and Computation*. 16:677–687.
43. Chen, Z., and T.L. Beck. 2016. Free Energies of Ion Binding in the Bacterial CLC-ec1 Chloride Transporter with Implications for the Transport Mechanism and Selectivity. *Journal of Physical Chemistry B*. 120:3129–3139.
44. Yue, Z., Z. Wang, and G.A. Voth. 2022. Ion permeation, selectivity, and electronic polarization in fluoride channels. *Biophysical Journal*.
45. Verkman, A.S., and L.J.V. Galietta. 2009. Chloride channels as drug targets. *Nature Reviews Drug Discovery*. 8:153–171.
46. Yu, J., H. Zhu, R. Lape, T. Greiner, J. Du, W. Lü, L. Sivilotti, and E. Gouaux. 2021. Mechanism of gating and partial agonist action in the glycine receptor. *Cell*. 184:957–968.
47. Laverty, D., R. Desai, T. Uchański, S. Masiulis, W.J. Stec, T. Malinauskas, J. Zivanov, E. Pardon, J. Steyaert, K.W. Miller, and A.R. Aricescu. 2019. Cryo-EM structure of the human α1β3γ2 GABAA receptor in a lipid bilayer. *Nature*. 565:516–520.

48. Yang, T., Q. Liu, B. Kloss, R. Bruni, R.C. Kalathur, Y. Guo, E. Kloppmann, B. Rost, H.M. Colecraft, and W.A. Hendrickson. 2014. Structure and selectivity in bestrophin ion channels. *Science*. 346:355–359.
49. Vaisey, G., A.N. Miller, and S.B. Long. 2016. Distinct regions that control ion selectivity and calcium-dependent activation in the bestrophin ion channel. *Proceedings of the National Academy of Sciences of the United States of America*. 113:E7399–E7408.
50. Xu, C., P. Lu, T.M. Gamal El-Din, X.Y. Pei, M.C. Johnson, A. Uyeda, M.J. Bick, Q. Xu, D. Jiang, H. Bai, G. Reggiano, Y. Hsia, T.J. Brunette, J. Dou, D. Ma, E. Lynch, S.E. Boyken, P.-S. Huang, L. Stewart, F. Dimaio, J.M. Kollman, B.F. Luisi, T. Matsuura, W.A. Catterall, and D. Baker. 2020. Computational Design of Transmembrane Pores. *Nature*. 585:129–134.
51. Su, J., and D. Huang. 2016. Coupling Transport of Water and Ions Through a Carbon Nanotube: The Role of Ionic Condition. *Journal of Physical Chemistry C*. 120:11245–11252.
52. Buchsbaum, S.F., M.L. Jue, A. Sawvel, C. Chen, E.R. Meshot, S.J. Park, M. Wood, K.J. Wu, C.L. Bilodeau, F. Aydin, T.A. Pham, Y. Edmond, F. Fornasiero, S.F. Buchsbaum, M.L. Jue, A. Sawvel, C. Chen, E.R. Meshot, and S.J. Park. 2020. Fast Permeation of Small Ions in Carbon Nanotubes. 2001802:1–61.
53. Zhu, F., and K. Schulten. 2003. Water and proton conduction through carbon nanotubes as models for biological channels. *Biophysical Journal*. 85:236–244.
54. García-fandiño, R., and M.S.P. Sansom. 2012. Designing biomimetic pores based on carbon nanotubes. *Proceedings of the National Academy of Sciences*. 109:6939–6944.
55. Amiri, H., K.L. Shepard, C. Nuckolls, and R. Hernández Sánchez. 2017. Single-Walled Carbon Nanotubes: Mimics of Biological Ion Channels. *Nano Letters*. 17:1204–1211.
56. Li, Y., Z. Li, F. Aydin, J. Quan, X. Chen, Y.-C. Yao, C. Zhan, Y. Chen, T.A. Pham, and A. Noy. 2020. Water-ion permselectivity of narrow-diameter carbon nanotubes. *Science Advances*. 6:1–9.
57. Li, Z., Y. Li, Y. Yao, F. Aydin, C. Zhan, Y. Chen, M. Elimelech, T.A. Pham, and A. Noy. 2020. Strong Differential Monovalent Anion Selectivity in Narrow Diameter Carbon Nanotube Porins. *ACS Nano*. 14:6269–6275.
58. Hummer, G., J.C. Rasaiah, and J.P. Noworyta. 2001. Water conduction through the hydrophobic channel of a carbon nanotube. *Nature*. 414:188–190.
59. Hanwell, M.D., D.E. Curtis, D.C. Lonie, T. Vandermeersch, E. Zurek, and G.R. Hutchison. 2012. Avogadro: an advanced semantic chemical editor, visualization, and analysis platform. *Journal of Cheminformatics*. 4:1–17.
60. Humphrey, W., A. Dalke, and K. Schulten. 1996. VMD: Visual Molecular Dynamics. *Journal of Molecular Graphics* . 14:33–38.
61. Klesse, G., S. Rao, M.S.P. Sansom, and S.J. Tucker. 2019. CHAP: A Versatile Tool for the Structural and Functional Annotation of Ion Channel Pores. *Journal of Molecular Biology*. 431:3353–3365.
62. Kandt, C., W.L. Ash, and D. Peter Tieleman. 2007. Setting up and running molecular dynamics simulations of membrane proteins. *Methods*. 41:475–488.
63. Abraham, M.J., T. Murtola, R. Schulz, S. Páll, J.C. Smith, B. Hess, and E. Lindah. 2015. Gromacs: High performance molecular simulations through multi-level parallelism from laptops to supercomputers. *SoftwareX*. 1–2:19–25.
64. Jorgensen, W.L., D.S. Maxwell, and J. Tirado-Rives. 1996. Development and Testing of the OPLS All-Atom Force Field on Conformational Energetics and Properties of Organic Liquids. *Journal of the American Chemical Society*. 118:11225–11236.
65. Fuentes-Azcatl, R., N. Mendoza, and J. Alejandre. 2015. Improved SPC force field of water based on the dielectric constant: SPC/ε. *Physica A: Statistical Mechanics and its Applications*. 420:116–123.
66. Hess, B., H. Bekker, H.J.C. Berendsen, and J.G.E.M. Fraaije. 1997. LINCS: A Linear Constraint Solver for Molecular Simulations. *J Comput Chem*. 18:1463–1472.
67. Darden, T., D. York, and L. Pedersen. 1993. Particle mesh Ewald: An N·log(N) method for Ewald sums in large systems. *The Journal of Chemical Physics*. 98:10089–10092.
68. Michaud-Agrawal, N., E.J. Denning, T.B. Woolf, and O. Beckstein. 2011. MDAnalysis: A toolkit for the analysis of molecular dynamics simulations. *Journal of Computational Chemistry*. 32:2319–2327.
69. Gowers, R.J.;, M.; Linke, J.; Barnoud, T. Reddy, E.; John, M.N.; Melo, S.L.; Seyler, J.; Domanski, D.L.; Dotson, S.; Buchoux, I.M.; Kenney, and O. Beckstein. 2016. MDAnalysis: A Python Package for the Rapid Analysis of Molecular Dynamics Simulations. In: Proc. of the 15th Python in Science Conf. . pp. 98–105.

70. Harris, C.R., K.J. Millman, S.J. van der Walt, R. Gommers, P. Virtanen, D. Cournapeau, E. Wieser, J. Taylor, S. Berg, N.J. Smith, R. Kern, M. Picus, S. Hoyer, M.H. van Kerkwijk, M. Brett, A. Haldane, J.F. del Río, M. Wiebe, P. Peterson, P. Gérard-Marchant, K. Sheppard, T. Reddy, W. Weckesser, H. Abbasi, C. Gohlke, and T.E. Oliphant. 2020. Array programming with NumPy. *Nature*. 585:357–362.
71. Dämgen, M.A., and P.C. Biggin. 2020. A Refined Open State of the Glycine Receptor Obtained via Molecular Dynamics Simulations. *Structure*. 28:130-139.e2.
72. Zhu, F., and G. Hummer. 2009. Gating transition of pentameric ligand-gated ion channels. *Biophysical Journal*. 97:2456–2463.
73. Leung, K., S.B. Rempe, and C.D. Lorenz. 2006. Salt permeation and exclusion in hydroxylated and functionalized silica pores. *Physical Review Letters*. 96.
74. Liang, Z.F., S.L. Ma, H.T. Xue, F. Ding, J.L. Liu, and F.L. Tang. 2018. Charge distribution in graphene from quantum calculation. *Chinese Physics B*. 27.
75. Sun, L., X. Li, Y. Tu, and H. Ågren. 2015. Origin of ion selectivity at the air/water interface. *Physical Chemistry Chemical Physics*. 17:4311–4318.
76. Jiménez-Ángeles, F., K.J. Harmon, T.D. Nguyen, P. Fenter, and M.O. de La Cruz. 2020. Nonreciprocal interactions induced by water in confinement. *Physical Review Research*. 2.
77. Kulik, H.J., E. Schwegler, and G. Galli. 2012. Probing the structure of salt water under confinement with first-principles molecular dynamics and theoretical X-ray absorption spectroscopy. *Journal of Physical Chemistry Letters*. 3:2653–2658.
78. Pham, T.A., S.M.G. Mortuza, B.C. Wood, E.Y. Lau, T. Ogitsu, S.F. Buchsbaum, Z.S. Siwy, F. Fornasiero, and E. Schwegler. 2016. Salt Solutions in Carbon Nanotubes: The Role of Cation-π Interactions. *Journal of Physical Chemistry C*. 120:7332–7338.
79. Aydin, F., A. Moradzadeh, C.L. Bilodeau, E.Y. Lau, E. Schwegler, N.R. Aluru, and T.A. Pham. 2021. Ion Solvation and Transport in Narrow Carbon Nanotubes: Effects of Polarizability, Cation-πInteraction, and Confinement. *Journal of Chemical Theory and Computation*. 17:1596–1605.
80. Leung, K., and M. Marsman. 2007. Energies of ions in water and nanopores within density functional theory. *Journal of Chemical Physics*. 127.
81. da Silva, L.B. 2014. Structural and dynamical properties of water confined in carbon nanotubes. *Journal of Nanostructure in Chemistry*. 4:1–5.
82. Köhler, M.H., J.R. Bordin, L.B. da Silva, and M.C. Barbosa. 2018. Structure and dynamics of water inside hydrophobic and hydrophilic nanotubes. *Physica A: Statistical Mechanics and its Applications*. 490:331–337.
83. Faucher, S., N. Aluru, M.Z. Bazant, D. Blankschtein, A.H. Brozena, J. Cumings, J. Pedro De Souza, M. Elimelech, R. Epsztein, J.T. Fourkas, A.G. Rajan, H.J. Kulik, A. Levy, A. Majumdar, C. Martin, M. McEldrew, R.P. Misra, A. Noy, T.A. Pham, M. Reed, E. Schwegler, Z. Siwy, Y. Wang, and M. Strano. 2019. Critical Knowledge Gaps in Mass Transport through Single-Digit Nanopores: A Review and Perspective. *Journal of Physical Chemistry C*. 123:21309–21326.
84. Mohammadzadeh, L., P. Quaino, and W. Schmickler. 2016. Interactions of anions and cations in carbon nanotubes. *Faraday Discussions*. 193:415–426.
85. Faucher, S., M. Kuehne, V.B. Koman, N. Northrup, D. Kozawa, Z. Yuan, S.X. Li, Y. Zeng, T. Ichihara, R.P. Misra, N. Aluru, D. Blankschtein, and M.S. Strano. 2021. Diameter Dependence of Water Filling in Lithographically Segmented Isolated Carbon Nanotubes. *ACS Nano*. 15:2778–2790.
86. Peng, X., Y. Zhang, H. Chu, Y. Li, D. Zhang, L. Cao, and G. Li. 2016. Accurate Evaluation of Ion Conductivity of the Gramicidin A Channel Using a Polarizable Force Field without Any Corrections. *Journal of Chemical Theory and Computation*. 12:2973–2982.
87. Ngo, V., H. Li, A.D. MacKerell, T.W. Allen, B. Roux, and S. Noskov. 2021. Polarization Effects in Water-Mediated Selective Cation Transport across a Narrow Transmembrane Channel. *Journal of Chemical Theory and Computation*. 17:1726–1741.
88. Dellostritto, M., J. Xu, X. Wu, and M.L. Klein. 2020. Aqueous solvation of the chloride ion revisited with density functional theory: Impact of correlation and exchange approximations. *Physical Chemistry Chemical Physics*. 22:10666–10675.
89. Powell, D.H., G.W. Neilson, J.E. Enderby, and D.H. Powellt. 1993. The structure of Cl-in aqueous solution: an experimental determination of g ClH (r) and g ClO (r). *Journal of Physics: Condensed Matter*. 5:5723–5730.
90. Bankura, A., V. Carnevale, and M.L. Klein. 2013. Hydration structure of salt solutions from ab initio molecular dynamics. *Journal of Chemical Physics*. 138:1–10.

91. Zhao, Z., D.M. Rogers, and T.L. Beck. 2010. Polarization and charge transfer in the hydration of chloride ions. *Journal of Chemical Physics*. 132.
92. Leung, K., S.B. Rempe, and O.A. von Lilienfeld. 2009. Ab initio molecular dynamics calculations of ion hydration free energies. *Journal of Chemical Physics*. 130.
93. Muralidharan, A., L.R. Pratt, M.I. Chaudhari, and S.B. Rempe. 2019. Quasi-chemical theory for anion hydration and specific ion effects: Cl-(aq) vs. F-(aq). *Chemical Physics Letters: X*. 4.
94. Enderby, J.E. 1985. Ionic hydration by neutron scattering. *Journal of Pure and Applied Chemistry*. 57:1025–1030.
95. Rowley, C.N., and B. Roux. 2012. The solvation structure of Na + and K + in liquid water determined from high level ab initio molecular dynamics simulations. *Journal of Chemical Theory and Computation*. 8:3526–3535.
96. Shi, Y., and T.L. Beck. 2020. Absolute ion hydration free energy scale and the surface potential of water via quantum simulation. *Proceedings of the National Academy of Sciences of the United States of America*. 117:30151–30158.
97. Varma, S., and S.B. Rempe. 2006. Coordination numbers of alkali metal ions in aqueous solutions. *Biophysical Chemistry*. 124:192–199.
98. Leontyev, I. v., and A.A. Stuchebrukhov. 2010. Electronic continuum model for molecular dynamics simulations of biological molecules. *Journal of Chemical Theory and Computation*. 6:1498–1508.
99. Kohagen, M., P.E. Mason, and P. Jungwirth. 2016. Accounting for Electronic Polarization Effects in Aqueous Sodium Chloride via Molecular Dynamics Aided by Neutron Scattering. *Journal of Physical Chemistry B*. 120:1454–1460.
100. Tůma, L., D. Jeníček, and P. Jungwirth. 2005. Propensity of heavier halides for the water/vapor interface revisited using the Amoeba force field. *Chemical Physics Letters*. 411:70–74.
101. Melcr, J., T. Mendes Ferreira, P. Jungwirth, and O.H.S. Ollila. 2019. Improved Cation Binding to Lipid Bilayer with Negatively Charged POPS by Effective Inclusion of Electronic Polarization. *Journal of Chemical Theory and Computation*. 16:738–748.
102. Ren, P., C. Wu, and J.W. Ponder. 2011. Polarizable atomic multipole-based molecular mechanics for organic molecules. *Journal of Chemical Theory and Computation*. 7:3143–3161.
103. Ren, P., and J.W. Ponder. 2003. Polarizable Atomic Multipole Water Model for Molecular Mechanics Simulation. 107:5933–5947.
104. McCaffrey, D.L., S.C. Nguyen, S.J. Cox, H. Weller, A.P. Alivisatos, P.L. Geissler, and R.J. Saykally. 2017. Mechanism of ion adsorption to aqueous interfaces: Graphene/water vs. air/water. *Proceedings of the National Academy of Sciences of the United States of America*. 114:13369–13373.
105. Kim, K., S.K. Kwon, S.H. Jun, J.S. Cha, H. Kim, W. Lee, J.F. Kim, and H.S. Cho. 2016. Crystal structure and functional characterization of a light-driven chloride pump having an NTQ motif. *Nature Communications*. 7:1–10.
106. Dickson, V.K., L. Pedi, and S.B. Long. 2014. Structure and insights into the function of a Ca2+-activated Cl- channel. *Nature*. 516:13–218.
107. Lisbjerg, M., H. Valkenier, B.M. Jessen, H. Al-Kerdi, A.P. Davis, and M. Pittelkow. 2015. Biotin[6]uril esters: Chloride-selective transmembrane anion carriers employing C-H···anion interactions. *Journal of the American Chemical Society*. 137:4948–4951.
108. Jing, Z., C. Liu, S.Y. Cheng, R. Qi, B.D. Walker, J.-P. Piquemal, and P. Ren. 2019. Polarizable Force Fields for Biomolecular Simulations: Recent Advances and Applications. *Annual Review of Biophysics*. 48:371–394.
109. Inakollu, V.S., D.P. Geerke, C.N. Rowley, and H. Yu. 2020. Polarisable force fields: what do they add in biomolecular simulations? *Current Opinion in Structural Biology*. 61:182–190.

Figure Legends

Figure 1: **A** Schematic of a biomimetic nanopore. The model nanopore has a radius r, such that $0 < r < R_{pore}$. **B** Top-down view of the pore, showing water molecules (blue) restrained to the CNT pore walls (orange) to create the polar regions at each mouth of the pore. The nanopore ends are capped with hydrogen atoms (white). **C** Snapshot of the simulation setup. The biomimetic nanopore is embedded in a POPC bilayer (lipid headgroup phosphates in green) and solvated with water (light blue), Cl^- (yellow) and Na^+ (pink). **D** Pore radius profile showing the maximum value of R_{pore} as a function of axial position *z* (approximately aligned with the simulation snapshot in **C)**.

Figure 2: Symmetrized number density profiles of Cl^- (**A** & **D**), Na^+ (**B** & **E**) and water (**C** & **F**), with ECC-rescaled ionic charges and a non-polarizable (NP) force field for all other atoms, at various salt concentrations. $\rho(r)/\rho_b$ represents the symmetrized number density, $\rho(r)$, sampled from the hydrophobic region of the nanopore (orange section of schematic (Fig. 1A)) and normalized by bulk density, ρ_b. The variable r is the radius of the nanopore which extends from 0 (pore axis) to R_{pore} (the interface where the salt solution meets the wall of the nanopore). The grey vertical dashed line represents R_{pore}.

Figure 3: Symmetrized number density profiles of Cl^- (**A** & **D**), Na^+ (**B** & **E**) and water (**C** & **F**), with ECC-rescaled ionic charges and a standard non-polarizable force field for all other atoms, in nanopores of different radii. $\rho(r)/\rho_b A$ represents the symmetrized number density, $\rho(r)$, sampled from the hydrophobic region of the nanopore and normalized by bulk density, ρ_b, and internal surface area, A, of the nanopore. The vertical dashed lines indicate the interface where the aqueous solution meets the wall of the nanopore (at radius R_{pore}) colored accordingly for each respective nanopore size.

Figure 4: Single-ion PMFs profiles for **A** Cl^- and **B** Na^+ permeating the model nanopore with ECC-rescaled ionic charges (green) and standard non-polarizable force field (yellow). The distance between the ion and the model nanopore center of mass is denoted by z where $z = 0$ represents the center of the pore. The solid lines indicate the free energy profile calculated from the final 5 ns of each umbrella window. Confidence bands were calculated by taking the standard error over independent 1 ns sampling blocks over the time period sampled. The dashed vertical lines denote the extent of the nanopore.

Figure 5: Cl^- hydration structure inside radial sections of the hydrophobic region of the pore. **A** Schematic of the hydrophobic region of the pore divided into four 0.175 nm radial sections colored in decreasing shades of blue. **B** & **D** The proportion of Cl^- with various hydration numbers in defined radial regions with the ECC method (**B**) and the non-polarizable force field (**D**). **C** shows the percentage occupancy of each radial section by Cl^-. With ECC (green line), Cl^- spends a significantly greater proportion of time within the interfacial layer whereas with the NP force field (orange line) Cl^- tends to occupy regions away from the pore wall.

Figure 6: **A** Snapshot of Cl^- partially desolvating to favorably interact with the internal hydrophobic interface of the model nanopore. Cl^- is represented in yellow and the oxygen atoms of the water molecules from the first and second hydration shells are represented by light and dark blue beads respectively. **B** Schematic diagram of an induced dipole in Cl^- at a hydrophobic/water interface. Adapted from (25).

Phan et al., Figure 1

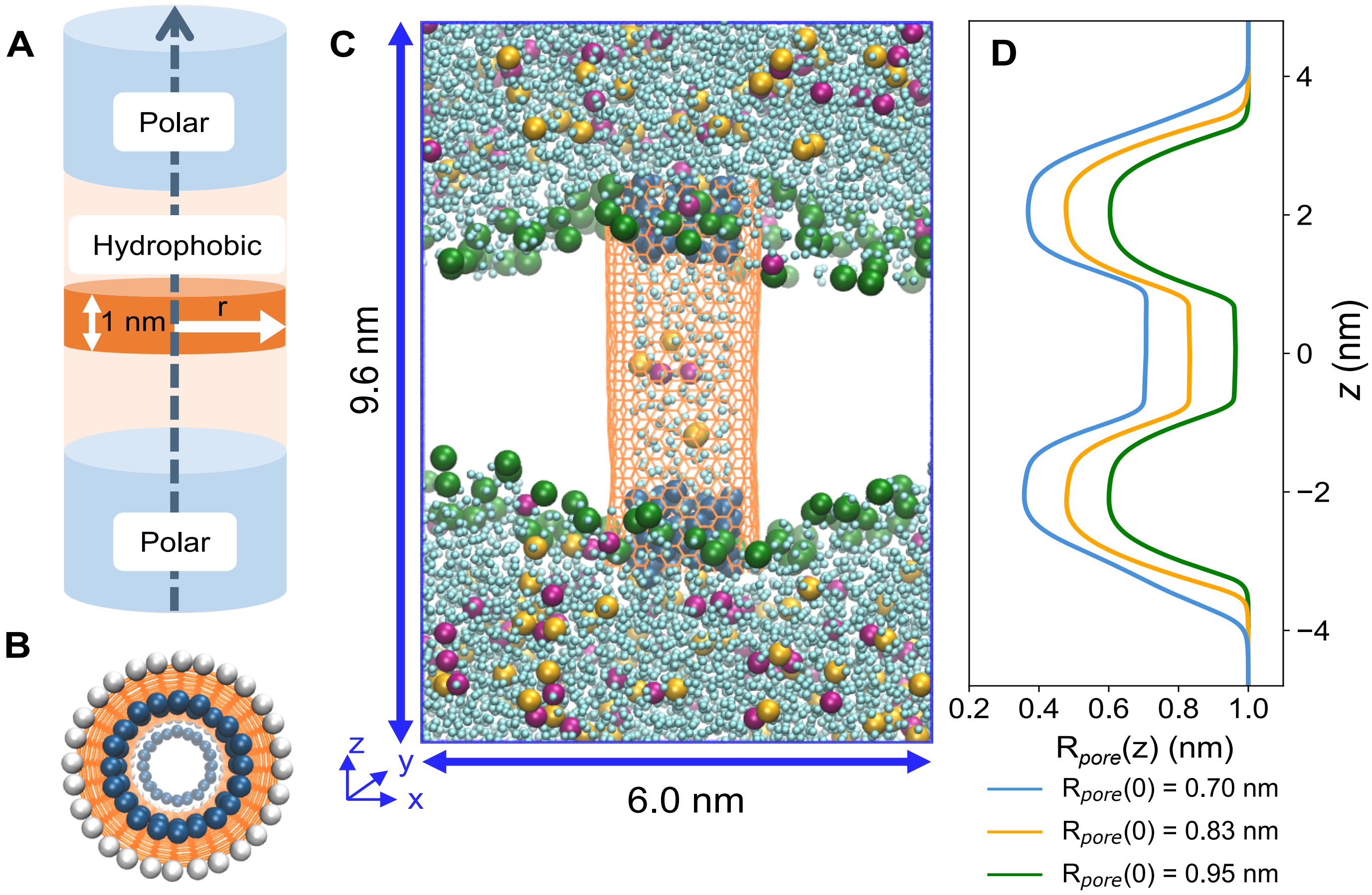

Phan et al., Figure 2

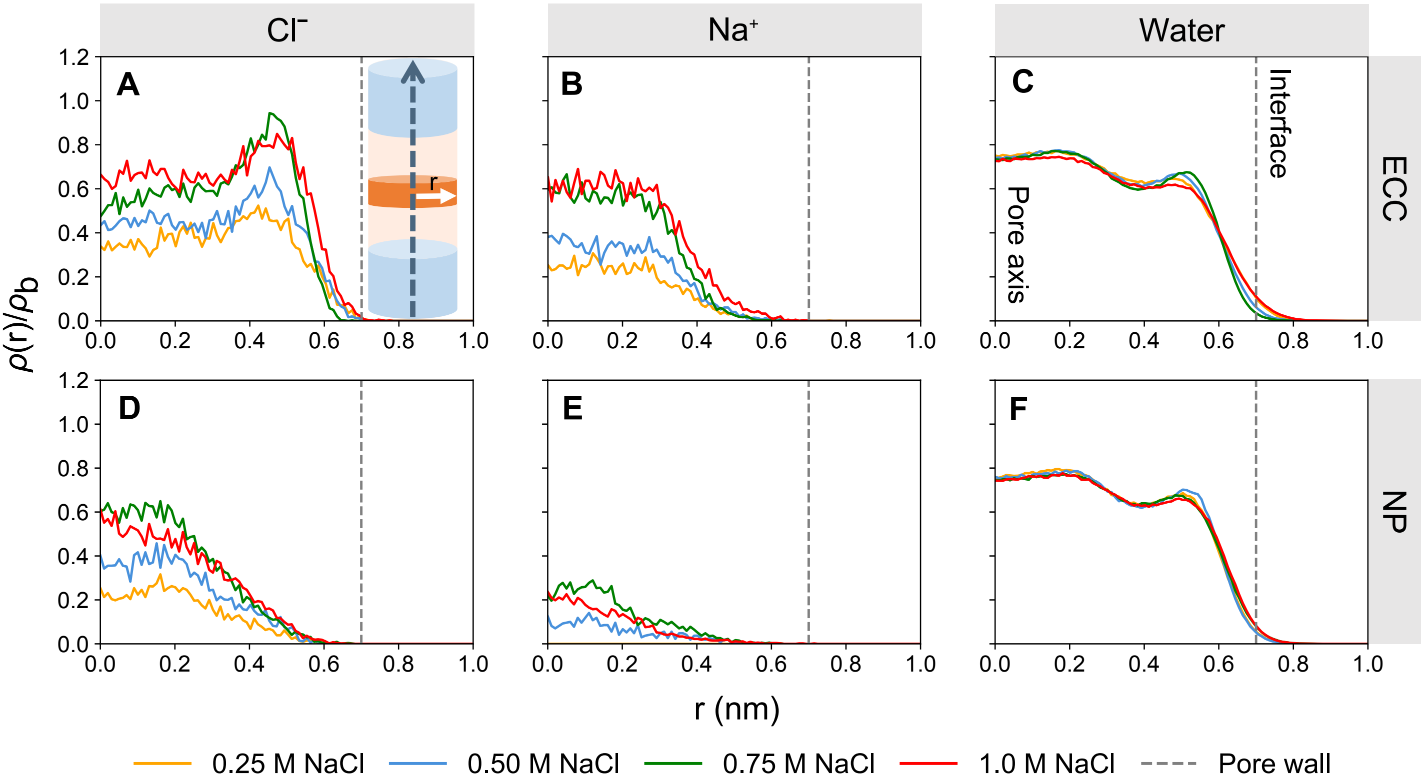

Phan et al., Figure 3

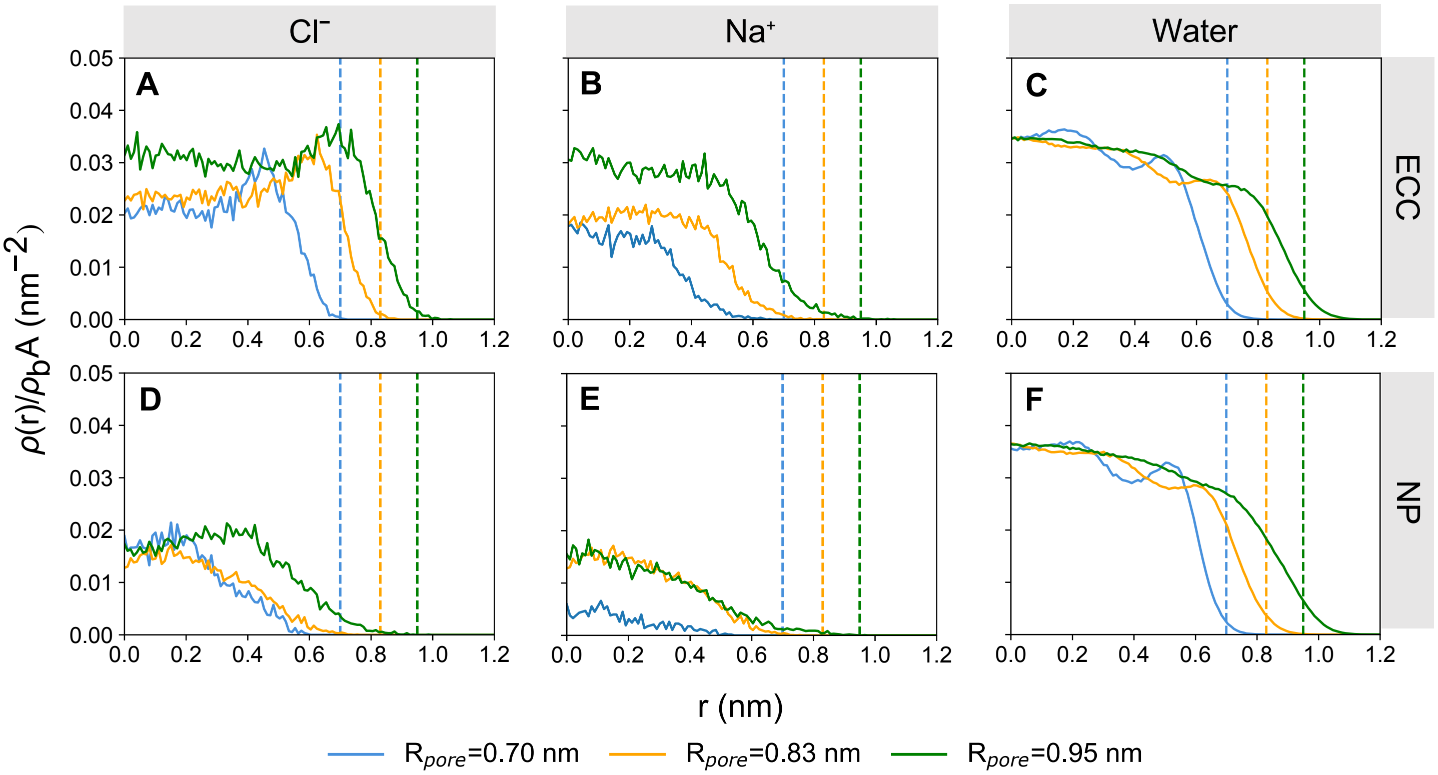

Phan et al., Figure 4

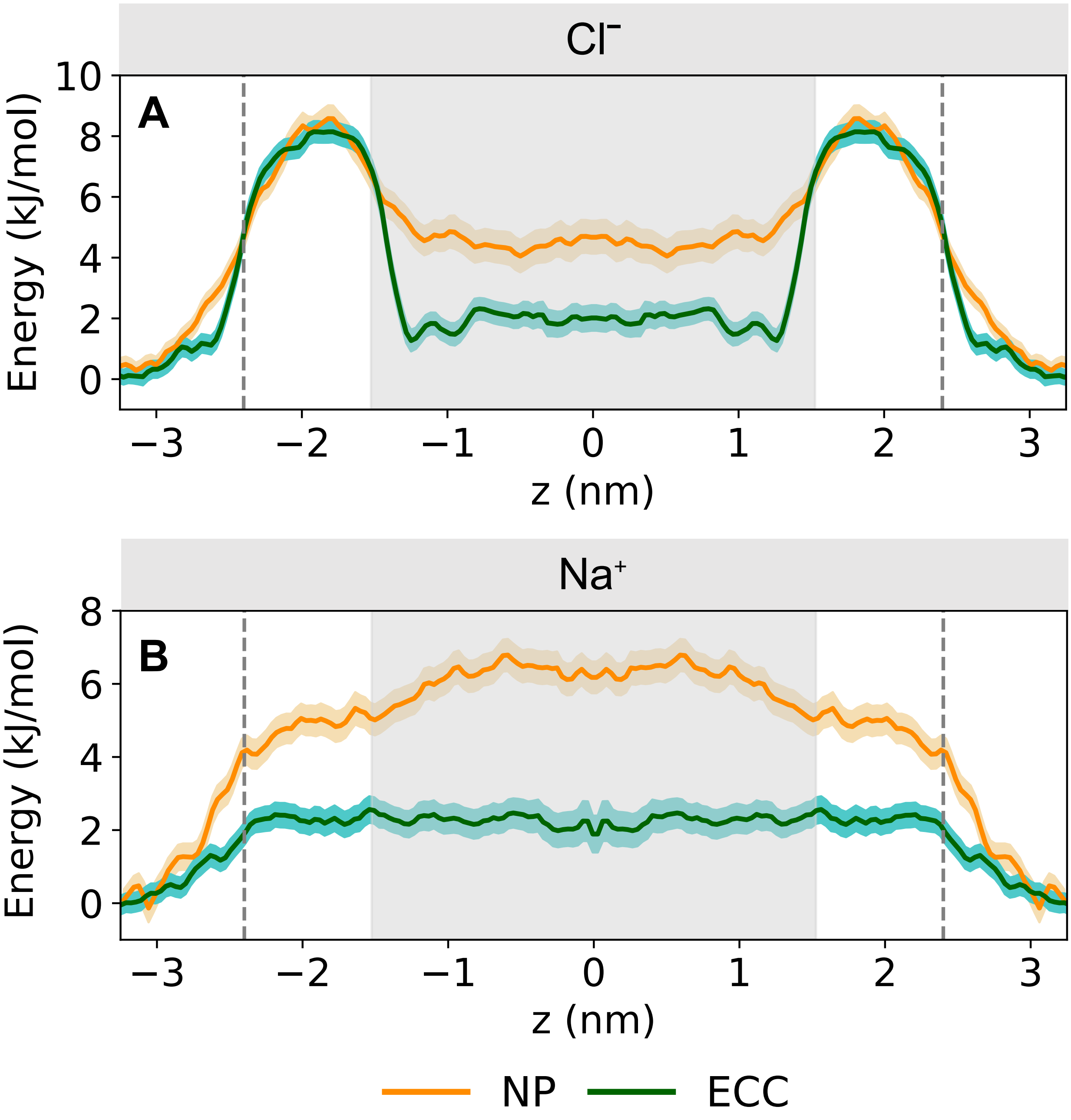

Phan et al., Figure 5

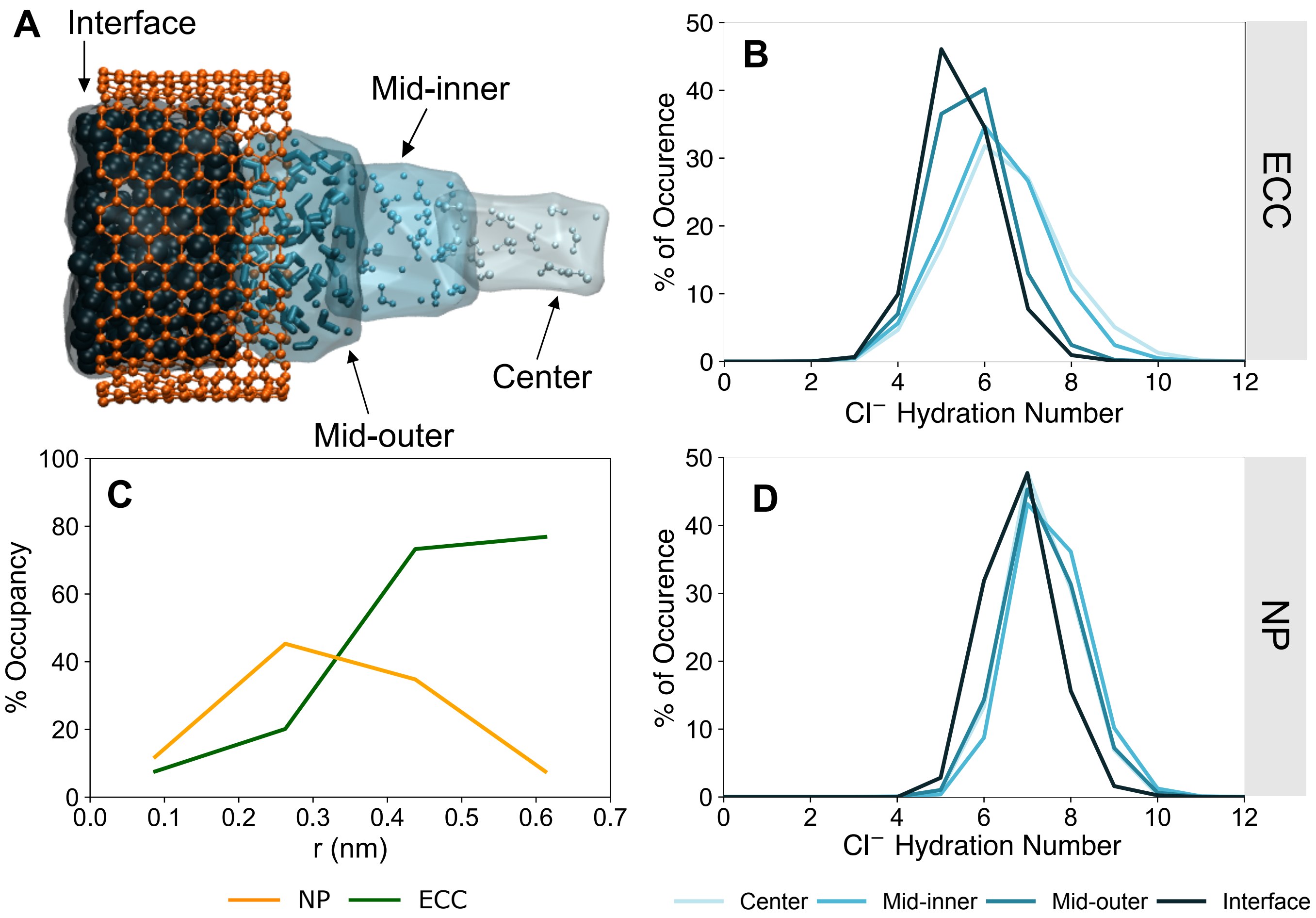

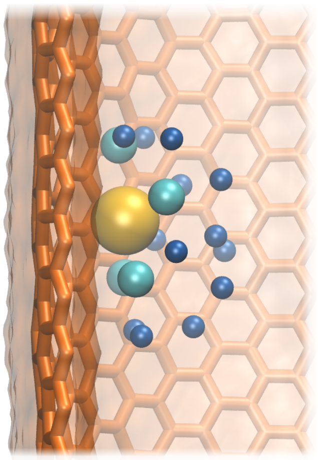
A

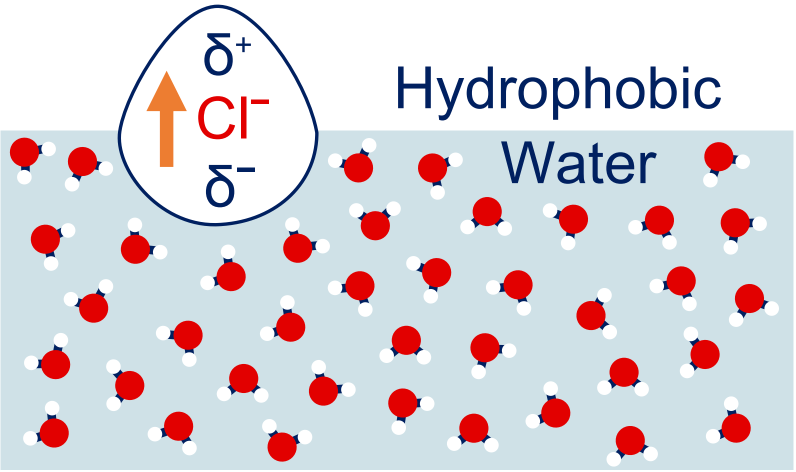
B
δ+
Cl−
δ−
Hydrophobic
Water

Supplemental Information

Influence of effective polarization on ion and water interactions within a biomimetic nanopore

Linda X. Phan[1,2], Charlotte I. Lynch[2], Jason Crain[2,3], Mark S.P. Sansom[2], Stephen J. Tucker[1,4*]*

[1] Clarendon Laboratory, Department of Physics, University of Oxford, Oxford, OX1 3PU, UK

[2] Department of Biochemistry, University of Oxford, Oxford, OX1 3QU, UK

[3] IBM Research Europe, Hartree Centre, Daresbury, WA4 4AD, UK

[4] Kavli Institute for Nanoscience Discovery, University of Oxford, OX1 3QU, UK

Supplemental Information

Figure S1

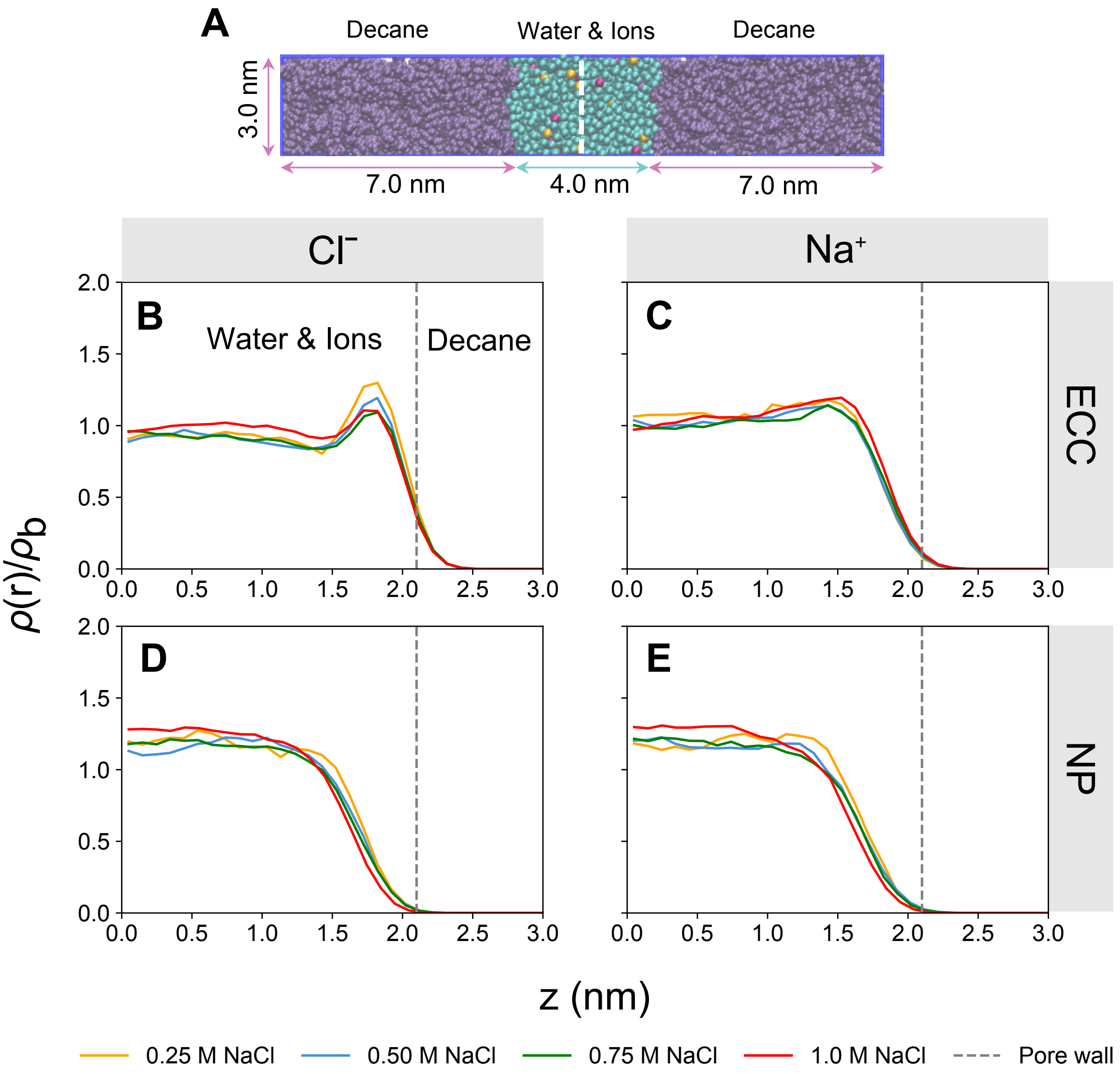

Figure S1: **A** Schematic of the aqueous/decane interface as a model slab system. The slab system consists of decane (purple), water (pale blue), Na^+ (pink) and Cl^- (yellow). Symmetrized number density profiles are shown for Cl^- (**B** & **D**) and Na^+ (**C** & **E**) at the aqueous/decane interface with ECC-rescaled charges and a non-polarizable force field at various salt concentrations. $\rho(r)/\rho_b$ represents the symmetrized number density, $\rho(r)$, which has been normalised by bulk density, ρ_b. The variable *z* is the distance from the center of the simulation box and the vertical dashed line corresponds to the aqueous/decane interface.

Figure S2

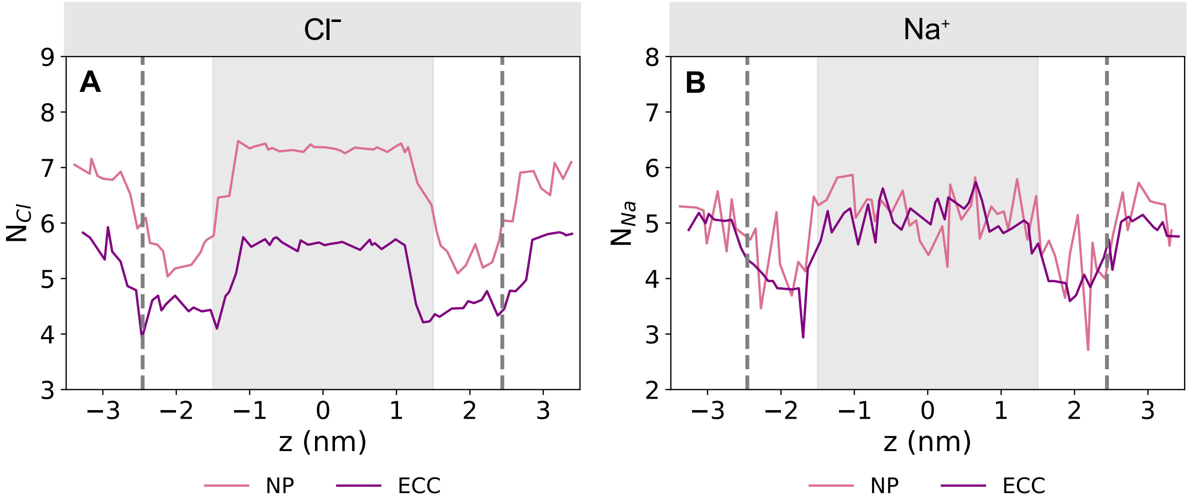

Figure S2: Variation in the first hydration shell of Cl⁻ (**A**) and Na⁺ (**B**) as a function of *z*, the distance between the ion and the model nanopore center of mass. N_{Cl} and N_{Na} denote the coordination number of water oxygen atoms in the first hydration shell of Cl⁻ and Na⁺ respectively, with ECC-rescaled ions (purple) and a non-polarizable (NP) force field (pink). The dashed vertical lines denote the extent of the nanopore.

Figure S3

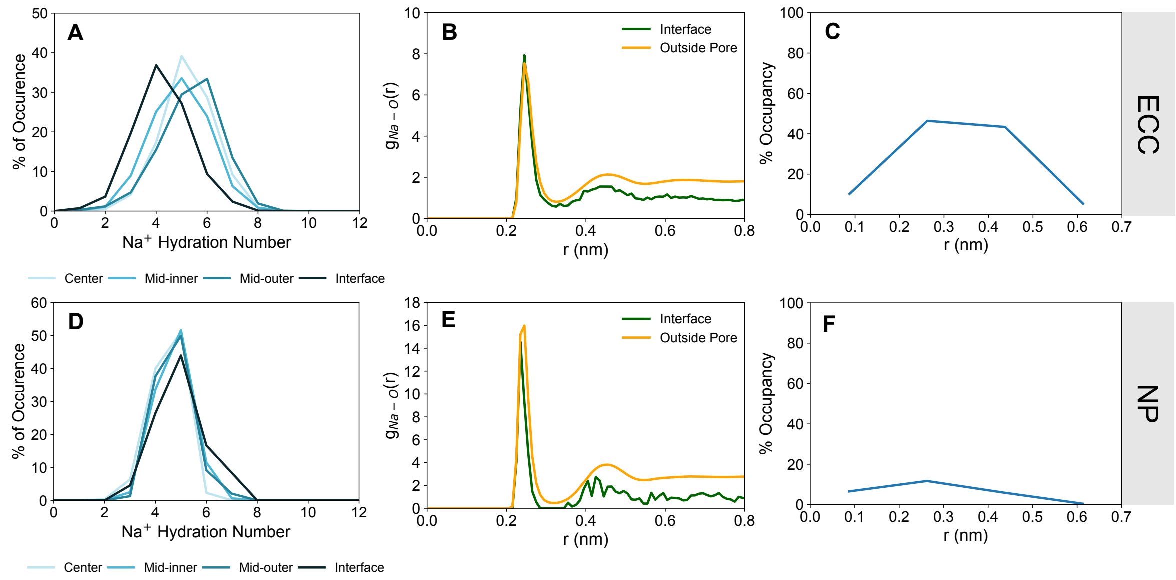

Figure S3: Na$^+$ hydration structure inside radial sections of the hydrophobic region of the pore with the ECC method and a non-polarizable (NP) force field. **A** & **D** show the proportion of Na$^+$ with various hydration numbers in defined radial regions for ECC and NP respectively. **B** & **E** show the radial distribution function of water oxygen atoms around Na$^+$ in the interfacial layer inside the pore (green) and outside the pore in bulk solution (yellow) for ECC and NP respectively. **C** & **F** show the percentage occupancy of each radial section by Na$^+$. With both ECC and the NP force field, Na$^+$ tend to occupy regions away from the hydrophobic pore interface.

Figure S4

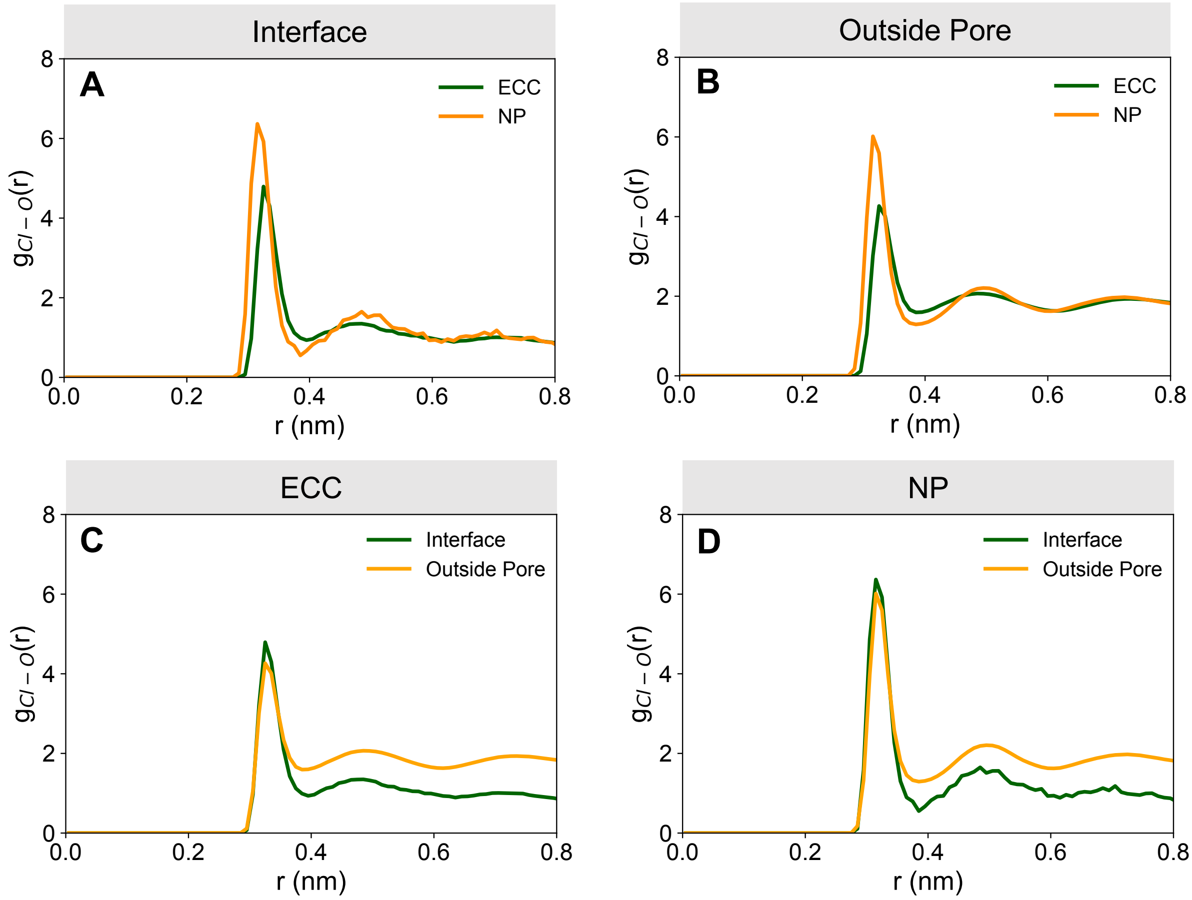

Figure S4: Radial distribution function (RDF), g_{Cl-O}(r), of water oxygen atoms around Cl^- at the interface (**A**) and outside the pore (**B**) with ECC and standard non-polarizable (NP) force field. **C** & **D** show the same RDFs as a comparison between the interface and outside the pore for a given force field parameter set.

Figure S5

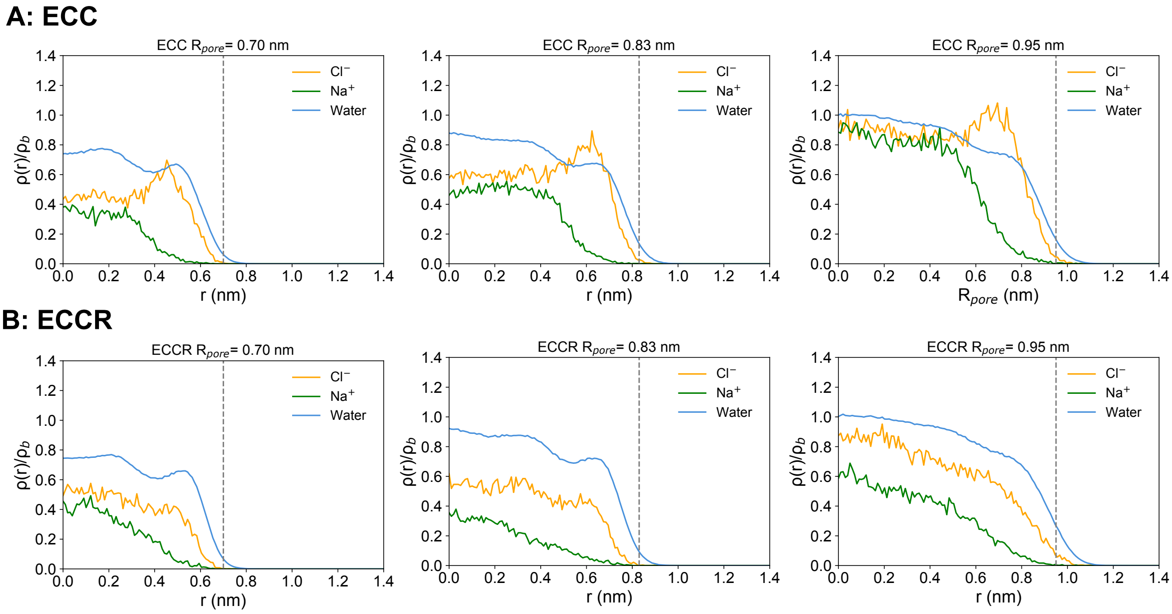

Figure S5: Symmetrized number density ($\rho(r)/\rho_b$) profiles of Cl^-, Na^+ and water, with ECC-rescaled ionic charges (**A**) and ECCR (**B**) (ECC with an additional small van der Waals radii rescaling) in nanopores of different radii. The variable r is the radius of the nanopore which extends from 0 (pore axis) to R_{pore} (the interface where the salt solution meets the wall of the nanopore). The grey vertical dashed lines represent R_{pore}.

Figure S6

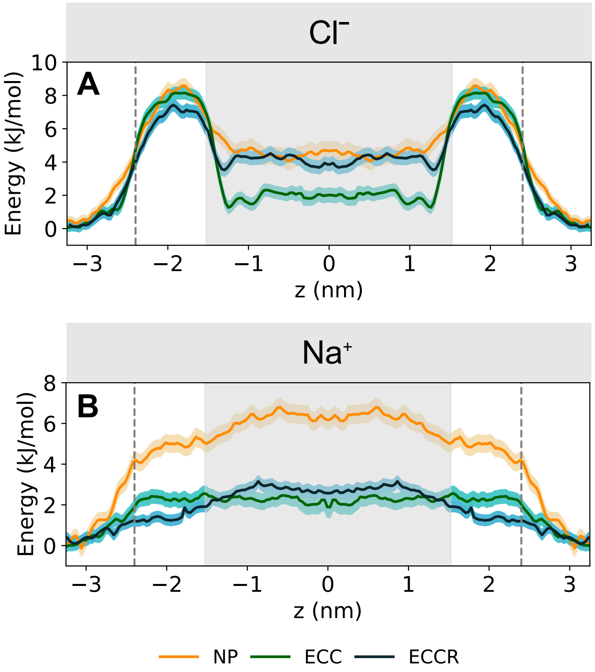

Figure S6: Single-ion PMF profiles for **A** Cl^- and **B** Na^+ permeating the model nanopore with ECC-rescaled ionic charges (green), standard non-polarizable (NP) force field (yellow) and ECCR (ECC with an additional small van der Waals radii rescaling) (dark blue). The distance between the ion and the model nanopore center of mass is denoted by z where $z = 0$ represents the center of the pore. The solid lines indicate the free energy profile calculated from the final 5 ns of each umbrella window. Confidence bands were calculated by taking the standard error over independent 1 ns sampling blocks over the time period sampled. The dashed vertical lines denote the extent of the nanopore.

Figure S7

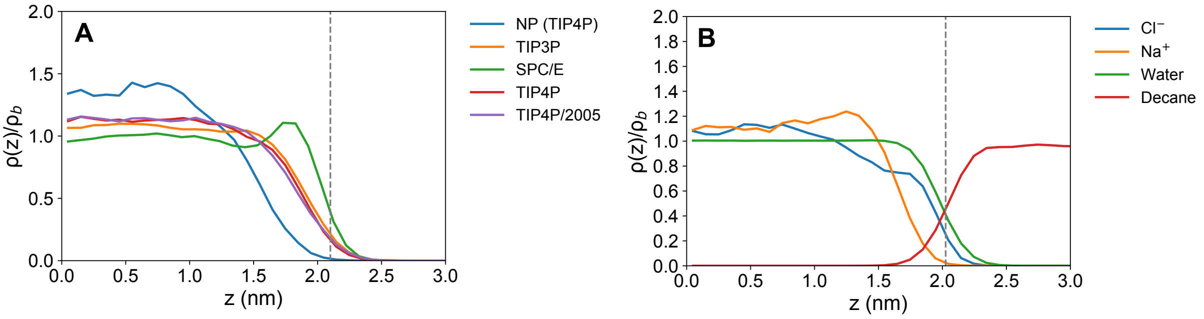

Figure S7: Symmetrized number density ($\rho(r)/\rho_b$) profiles for Cl⁻ (**A**) at an aqueous/decane interface employing various water models with ECC-rescaled charges and a non-polarizable (NP) force field using TIP4P water model. **B** shows the symmetrized number density profiles for Cl⁻, Na⁺ and water using the AMOEBA polarizable force field with the AMOEBA03 water model. The variable *z* is the distance from the center of the simulation box and the vertical dashed line denotes the aqueous/decane interface.

Figure S8

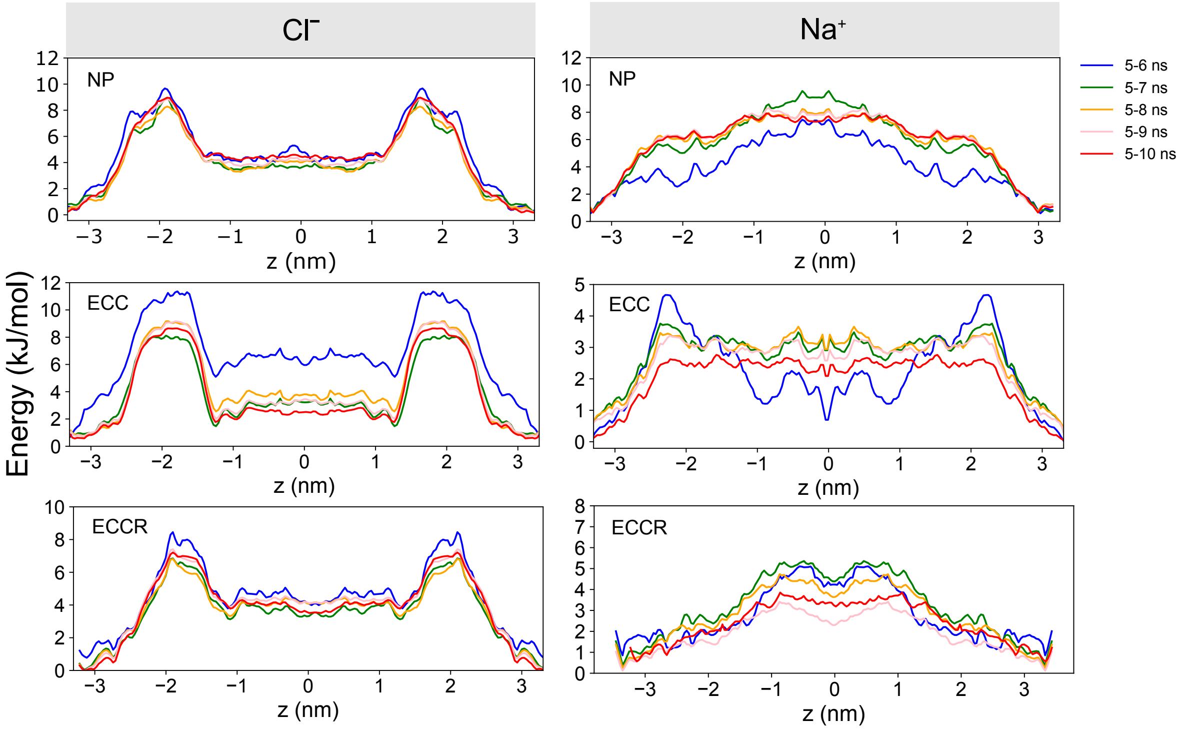

Figure S8: Single-ion PMFs convergence analysis for Cl⁻ and Na⁺ using a non-polarizable (NP) force field, ECC and ECCR ion parameters. Convergence analysis was performed by calculating 1 ns cumulative sampling blocks over the sampling time (last 5 ns of simulation).